

# Smart Nanoparticles as Advanced Anti-Akt Kinase Delivery Systems for Pancreatic Cancer Therapy

Juan Gonzalez-Valdivieso, Andres Garcia-Sampedro, Andrew R. Hall, Alessandra Girotti, Francisco Javier Arias, Stephen P. Pereira, and Pilar Acedo\*

Cite This: *ACS Appl. Mater. Interfaces* 2021, 13, 55790–55805

Read Online

ACCESS |

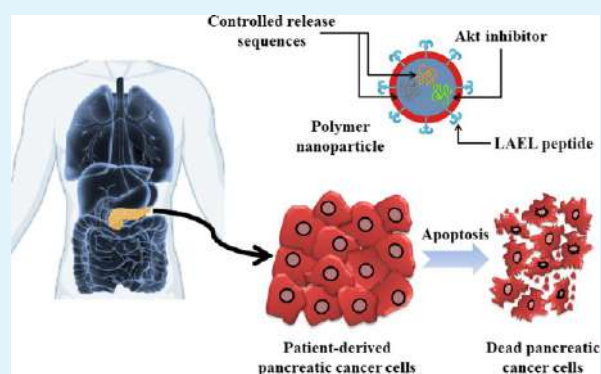
Metrics & More

Article Recommendations

Supporting Information

**ABSTRACT:** Pancreatic cancer is one of the deadliest cancers partly due to late diagnosis, poor drug delivery to the target site, and acquired resistance to therapy. Therefore, more effective therapies are urgently needed to improve the outcome of patients. In this work, we have tested self-assembling genetically engineered polymeric nanoparticles formed by elastin-like recombinamers (ELRs), carrying a small peptide inhibitor of the protein kinase Akt, in both PANC-1 and patient-derived pancreatic cancer cells (PDX models). Nanoparticle cell uptake was measured by flow cytometry, and subcellular localization was determined by confocal microscopy, which showed a lysosomal localization of these nanoparticles. Furthermore, metabolic activity and cell viability were significantly reduced after incubation with nanoparticles carrying the Akt inhibitor in a time- and dose-dependent fashion. Self-assembling  $73 \pm 3.2$  nm size nanoparticles inhibited phosphorylation and consequent activation of Akt protein, blocked the NF- $\kappa$ B signaling pathway, and triggered caspase 3-mediated apoptosis. Furthermore, *in vivo* assays showed that ELR-based nanoparticles were suitable devices for drug delivery purposes with long circulating time and minimum toxicity. Hence, the use of these smart nanoparticles could lead to the development of more effective treatment options for pancreatic cancer based on the inhibition of Akt.

**KEYWORDS:** nanoparticle, drug delivery, elastin-like recombinamer, Akt, pancreatic cancer



## 1. INTRODUCTION

Pancreatic ductal adenocarcinoma (PDAC) remains one of the deadliest cancers despite the different treatments developed during the last years.<sup>1,2</sup> Different factors are associated with its late diagnosis, poor prognosis, and low success of treatment options available for this disease, such as the difficulty to reach the tumor site, damage to healthy tissues or the ability of pancreatic cancer cells to acquire resistance to therapeutics.<sup>3–5</sup> Therefore, novel therapeutic strategies are urgently needed to achieve higher treatment efficacy, minimizing disease relapse and undesired effects on healthy tissues.<sup>5–7</sup> Biomaterials have become one of the most promising therapeutic approaches for drug delivery purposes, to achieve a more specific and controlled action, overcoming the poor accumulation of current drugs in the desmoplastic pancreatic tumors.<sup>8</sup>

Among biomaterials, elastin-like recombinamers (ELRs) stand out due to their biocompatibility, biodegradability, and stimuli responsive behavior. ELRs are polymeric biomaterials composed by the repetition of the VPGXG pentapeptide found in the sequence of natural elastin, where X represents any amino acid except proline.<sup>9</sup> ELRs are created by genetic engineering techniques, which allow us to control the amino acid sequence and to add a variety of bioactive sequences to

regulate their interaction with different cellular components.<sup>10</sup> Elastin-based polymers are characterized by their inverse temperature transition (ITT), which determines the transition temperature ( $T_t$ ) below which the polymeric chains remain as soluble disordered molecules in aqueous solution. However, when the temperature is increased above the  $T_t$ , the chains adopt an ordered  $\beta$ -spiral conformation resulting in their self-assembly in coacervates.<sup>11</sup> This whole process is completely reversible and depends on the amino acid composition, sequence, temperature, pH, ions, or light. Due to their stimuli-responsiveness behavior, ELR-based polymers are promising tools for biomedical applications, especially for controlled drug delivery.<sup>12–14</sup>

Biomaterials allow us to improve the biodistribution and circulating time of drugs in the bloodstream, and, in particular, nanoparticles (NPs) have emerged as an interesting strategy to

Received: August 1, 2021

Accepted: November 5, 2021

Published: November 17, 2021



achieve a controlled drug release in targeted tissues.<sup>15,16</sup> Moreover, NPs have been shown to avoid unspecific drug accumulation in vital organs, thereby allowing the use of higher concentrations of chemotherapeutic agents.<sup>15,17</sup> In addition, tumors are characterized by the enhanced permeability and retention (EPR) effect, which enhances vascular permeability and the retention of drugs in the tumor site.<sup>18,19</sup>

Specific cancerous markers are usually chosen to improve the selective accumulation and action of chemotherapeutic agents and to decrease the effect on non-cancerous cells due to their overexpression on cancerous cells compared to healthy tissues.<sup>20,21</sup> We selected the Akt kinase as our target protein for this study as Akt is overexpressed in different cancer cells including pancreatic, breast, and colorectal, among others.<sup>22</sup> Akt plays a pivotal role in cancer progression and chemoresistance, as it is involved in multiple key processes such as cell growth, proliferation and survival via different signaling pathways.<sup>23,24</sup> It has been shown that pancreatic cancer cells have a higher expression of activated, phosphorylated Akt kinase than normal pancreatic cells to promote cell proliferation and to avoid apoptosis-mediated cell death. In normal cells, Akt remains inactivated and the kinase is only phosphorylated, in response to external stimuli, such as growth factors.<sup>3,25</sup>

The Akt protein is activated after a conformational change triggered by lipid products of phosphoinositide-3-kinase (PI3K) and phosphorylation at threonine 308 and serine 473 residues.<sup>26</sup> This mechanism of Akt activation is well known, and different molecules have been designed to inhibit Akt phosphorylation as therapeutic approaches at the molecular level.<sup>27</sup> Among these molecules, a small 15 amino acid peptide inhibitor discovered by Hiromura *et al.*,<sup>28</sup> Akt-in, appeared as an effective tool for the blockade of the Akt signaling pathway by avoiding phosphatidylinositol triphosphate moieties binding to Akt protein and, as a consequence, preventing the activation of Akt kinase. In fact, the peptide showed *in vitro* inhibition of cell proliferation and anti-apoptotic activity and *in vivo* tumor regression.<sup>28</sup> The here-proposed ELR NPs carry this Akt inhibitor (Akt-in) to facilitate its entrance into the cellular cytoplasm, avoid its degradation, and improve its therapeutic effect in pancreatic cancer cells.

One of the reasons for the low success rate of different clinical trials for PDAC is the wide intratumoral heterogeneity of pancreatic tumors. *In vitro* cell cultures consisting of established cell lines are an important limiting factor as cells arise from the same single clone, not fully representing the characteristic genetic heterogeneity of a tumor. For this reason, in this work, we have used two different clinically relevant pancreatic cancer patient-derived cells, previously described as PDX185 and PDX354 cells.<sup>29–31</sup> Patient-derived models allow us to study novel therapeutic drugs in more physiological conditions including different cancer cell populations and cancer stem cells.<sup>32–34</sup>

In the present work, we have studied the effect of a novel therapeutic treatment based on smart self-assembling ELR NPs for controlled and precise drug delivery of an Akt inhibitor to patient-derived pancreatic cancer cells. Although these ELR NPs were previously characterized and studied in breast and colorectal *in vitro* cancer cell cultures,<sup>35</sup> this is the first time these NPs have been evaluated as a novel strategy for PDAC therapy, in patient-derived models, as a first step toward the development of a novel therapy. Therefore, we developed an advanced nanocarrier for controlled drug delivery, which could

be a promising treatment for pancreatic cancer in combination with chemotherapy.

## 2. RESULTS AND DISCUSSION

### 2.1. ELRs Design and Physicochemical Characterization.

ELRs are able to self-assemble into different structures, depending on their composition, above their Tt.<sup>36</sup> In this work, two different polymers were used, both consisting of an amphiphilic backbone formed by a glutamic acid-based hydrophilic block and an isoleucine-containing hydrophobic block (Figure 1). Our therapeutic construct included an Akt-in

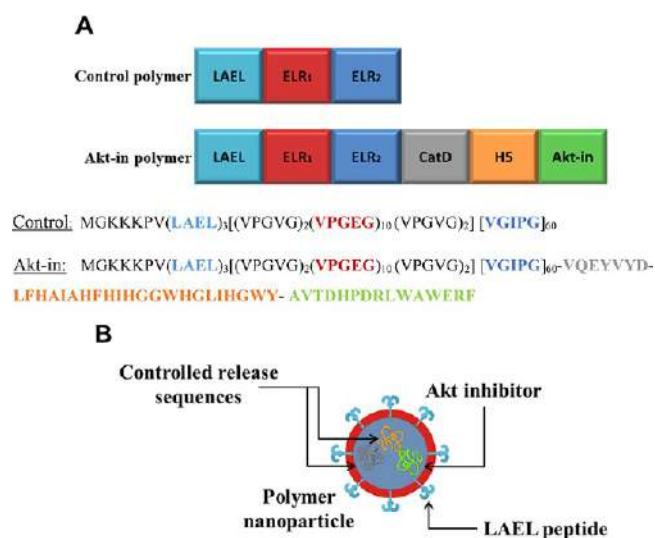


**Figure 1.** Scheme of ELR composition. (A) The different blocks forming ELR-based polymers are represented in a non-scaled scheme. LAEL sequence facilitates the NP internalization into the cells. ELR<sub>1</sub> is a hydrophilic block containing isoleucine as a guest residue. ELR<sub>2</sub> is a block containing glutamic acid. Cathepsin D-sensitive sequence is recognized by lysosomal proteases and H5 peptide allows the escape of the Akt inhibitor (green block) from the endo/lysosomes at acidic pH. Amino acid sequence of ELR polymers: the color code identifies the functional peptides of the molecules. (B) Scheme of the nanoparticle structure.

peptide, which inhibits the phosphorylation of the protein kinase Akt at serine 473.<sup>28,35</sup> This step is key for Akt cytoplasmic activation and its kinase activity regulating multiple signaling pathways.<sup>25</sup> Moreover, other bioactive sequences were added in order to allow the controlled release of the therapeutic inhibitor in the target cells. The LAEL sequence was included to facilitate the internalization of the NPs into the cells and to escape from the endosomes/lysosomes, where they accumulate, and often, drugs get inactivated before they can reach their target.<sup>37</sup> Also, a cathepsin D-sensitive sequence exclusively recognized by lysosomal proteases<sup>38</sup> and the sequence encoding the H5 peptide<sup>39</sup> were added to allow the escape of the Akt inhibitor from the endo/lysosomes.

The control ELR construct only contained the LAEL sequence and was used to clarify any cytotoxicity resulting from the ELR modules, the internalization of the NPs, and their escape from endo/lysosomes. Both ELR polymers included three lysine residues at the N-terminus, to which different molecules could be linked by covalent binding.

The physicochemical characterization of the two polymers used, and previously described by us, was validated as shown in

Table 1. Physicochemical Characterization of ELR Polymers<sup>a</sup>

	polymer			nanoparticle		
	predicted molecular weight (Da)	experimental molecular weight (Da)	Tt (°C)	D <sub>h</sub> (nm)	PdI	ζ-potential (mV)
control	48,250	48,240	15.59	67.1 ± 2.5	0.093	-27.6 ± 1.3
Akt-in	55,330	55,390	15.23	73.1 ± 3.2	0.083	-26.7 ± 1.7

<sup>a</sup>Experimental molecular weights were determined by MALDI-TOF/MS. Transition temperatures (Tt) of ELRs dissolved in PBS were measured by DSC. The size (diameter, D<sub>h</sub>) and polydispersity index (PdI) of self-assembled NPs dissolved in PBS were measured by DLS at 37 °C. NP ζ-potential dissolved in ultrapure water type I was measured by DLS at 37 °C. *n* = 3 independent experiments, mean ± SD.

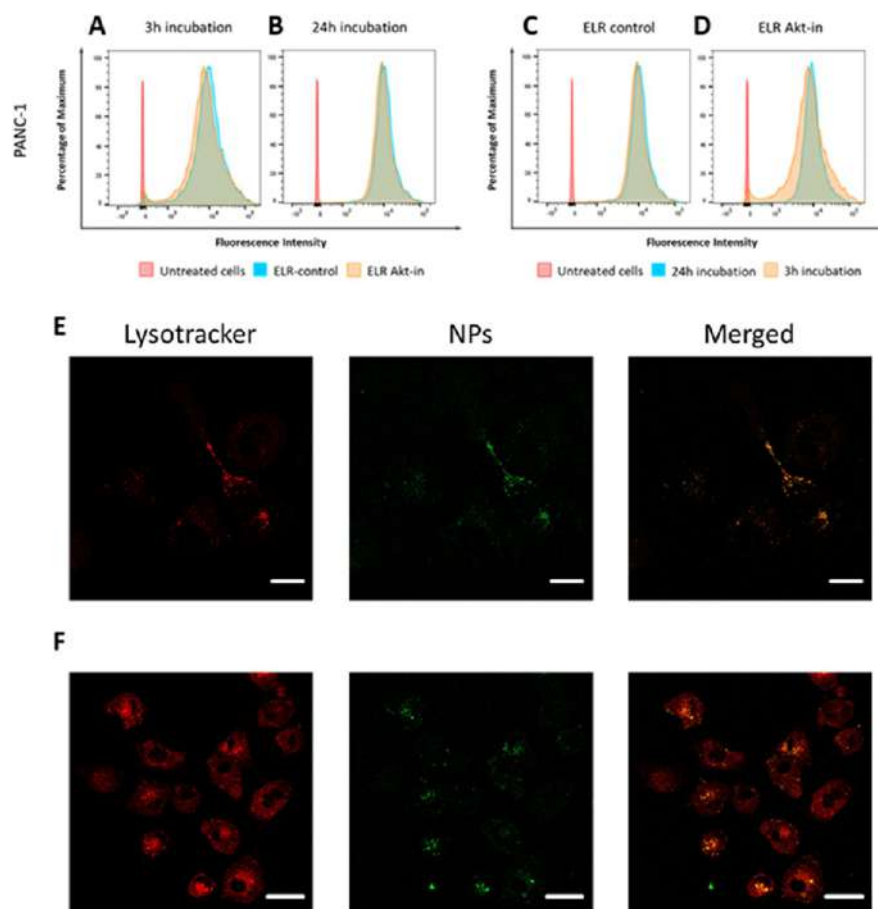


**Figure 2.** Cellular uptake and subcellular localization of ELR-based nanoparticles in PANC-1 cells. (A, B) Flow cytometry analysis of cells incubated with 0.5 mg/mL Cy5-labeled control and Akt-in NPs (blue and orange histograms, respectively) for 3 (A) or 24 h (B). *n* = 3 independent experiments. (C, D) Flow cytometry time-course analysis of cells incubated with 0.5 mg/mL Cy5-labeled control (C) or Akt-in NPs (D) for 3 (orange histogram) or 24 h (blue histogram). Untreated cells are plotted as red histograms. *n* = 3 independent experiments. (E, F) Confocal microscopy images of PANC-1 cells containing fluorescein-labeled nanoparticles (green channel) after 3 (E) or 24 h (F) incubation. Lysosomes were stained with LysoTracker Red dye (red channel). The overlap of the green and red channels resulted in yellow fluorescence. Scale bars: 15 (E) and 25 μm (F).

Figures S1 and S2.<sup>35</sup> Control and Akt-in polymers showed a similar Tt of 15.59 and 15.23 °C, respectively (Figures S1C and S2C), indicating the minor influence of the bioactive sequences (LAEL, CatD, and H5) in their smart behavior. DLS results showed that the control and the Akt-in polymers were able to self-assemble into 73.1 ± 3.2 and 67.1 ± 2.5 nm-size monodisperse particles, respectively (Figures S3A and S4A). Figures S3B and S4B show the negative surface charge of the NPs (-27 mV) due to the hydrophilic block containing glutamic acid forming the corona. On the other hand, when polymers were fluorescently labeled, neither the NP size nor surface charge was altered (Table S2). In conclusion, these results confirmed the high reproducibility of our nanoconstructs

and showed that our ELR-based NPs fit all the requirements for their application as drug delivery systems (Table 1).

**2.2. Cellular Uptake and Localization of ELR Nanoparticles.** The NP cellular uptake by pancreatic cancer cells was determined by flow cytometry (Figure 2 and Figure S5). PANC-1, PDX185, and PDX354 cells were incubated with Cy5-labeled control or Akt-in NPs at 0.5 mg/mL for 3 or 24 h. Surface charge affects the internalization rate of a nanodevice through the cellular membrane. The cellular membrane possesses a negative charge, so neutral and negatively charged NPs are thought to be internalized via endocytic pathways.<sup>40</sup> Conversely, cationic carriers tend to cause membrane depolarization and disruption,<sup>41</sup> leading to a reduction of viability of normal cells. Moreover, cationic NPs are more

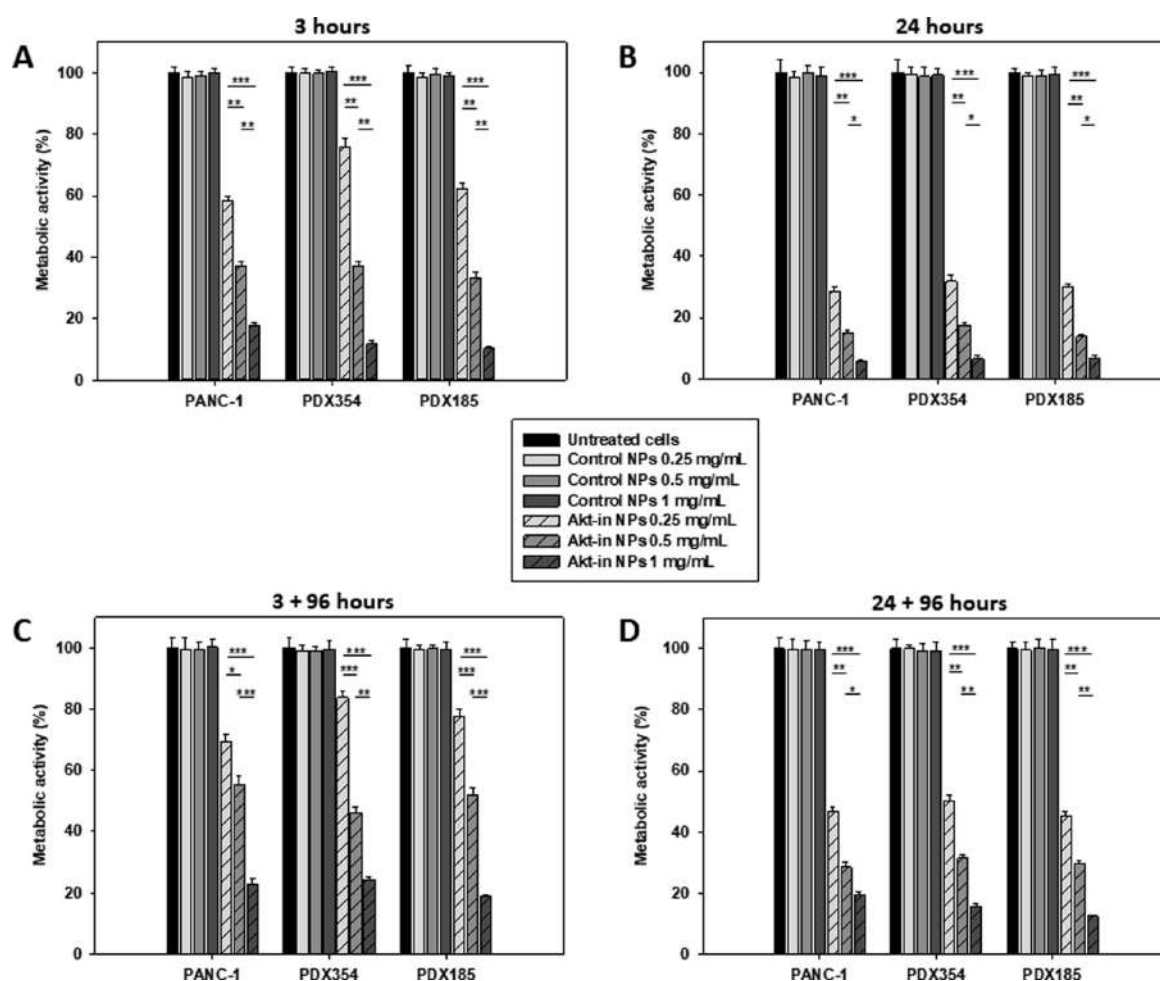


**Figure 3.** Metabolic activity of PANC-1, PDX354, and PDX185 cells after treatment with ELR-based nanoparticles. (A, B) Cells were incubated with three concentrations of control and Akt-in nanoparticles for 3 (A) or 24 h (B), and metabolic activity was measured following treatment with NPs using the MTT assay. (C, D) Cells were incubated with three concentrations of control and Akt-in nanoparticles for 3 (C) or 24 h (D), media was replaced, and metabolic activity was measured after 96 h.  $n = 3$  independent experiments, each in triplicate. Mean  $\pm$  SD. \* $p < 0.05$ ; \*\* $p < 0.01$ ; \*\*\* $p < 0.001$ .

likely to form aggregates by interacting with proteins present in biological fluids such as blood, increasing their size due to protein corona formation before they reach the target site.<sup>42,43</sup>

Flow cytometry data (Figure 2 and Figure S5) showed overlapping histograms for cells treated with Cy5-labeled control and Akt-in NPs. This suggests that the uptake rate for both nanocarriers is similar, as no significant differences between both types of NPs were observed. The fluorescence intensity observed in cells treated for 3 h with NPs was almost identical to 24 h treatment, indicating that the internalization of the designed NPs occurred in a short period of time (3 h) after which a minimal increase in uptake was detected. A similar trend was observed among all cell types analyzed. Therefore, we can conclude that both control and Akt-in NPs were internalized at a similar rate and the posterior differences detected in cell viability and metabolic activity were only due to the presence of the Akt kinase inhibitor. In Figure 2C,D, cellular uptake of ELR control and Akt-in NPs over time was depicted. Interestingly, a similar amount of ELR NPs was internalized after a 3 or 24 h incubation period. Moreover, PANC-1 cells showed lower internalization rates than patient-derived pancreatic cancer cells, which could be explained by the higher aggressiveness of primary tumor cells compared to

established cell lines, displaying an enhanced metabolic activity and internalization rate.

Next, confocal microscopy was carried out to study the subcellular localization and accumulation of the NPs (Figure 2E,F). ELR NPs were accumulated inside the cells and their green fluorescence signal co-localized with lysosomes (labeled in red with the lysosomal probe LysoTracker Red). Intracellular lysosomal localization was essential for the accurate action of our nanoconstructs, as the cathepsin D-sensitive sequence included in the ELR needs to be recognized by the lysosomal proteases to facilitate the release of the Akt-in. Moreover, at acidic lysosome pH, the H5 peptide included in the ELRs is designed to trigger the formation of pores in the lysosomal membrane, allowing the small Akt inhibitor to be released to the cytoplasm. All of these concatenated steps are the key for the effective ELR NP anti-tumor action. If NPs were not internalized into the lysosomes, the Akt inhibitor would not be released to the cytoplasm and could never reach the target Akt protein. There were no differences in terms of the subcellular localization of NPs in PANC-1 and PDX cells (data not shown).

**2.3. Effect of Nanoparticles on Cellular Metabolic Activity.** Once the uptake and the localization of the NPs were determined, their cytotoxic effect was analyzed. A

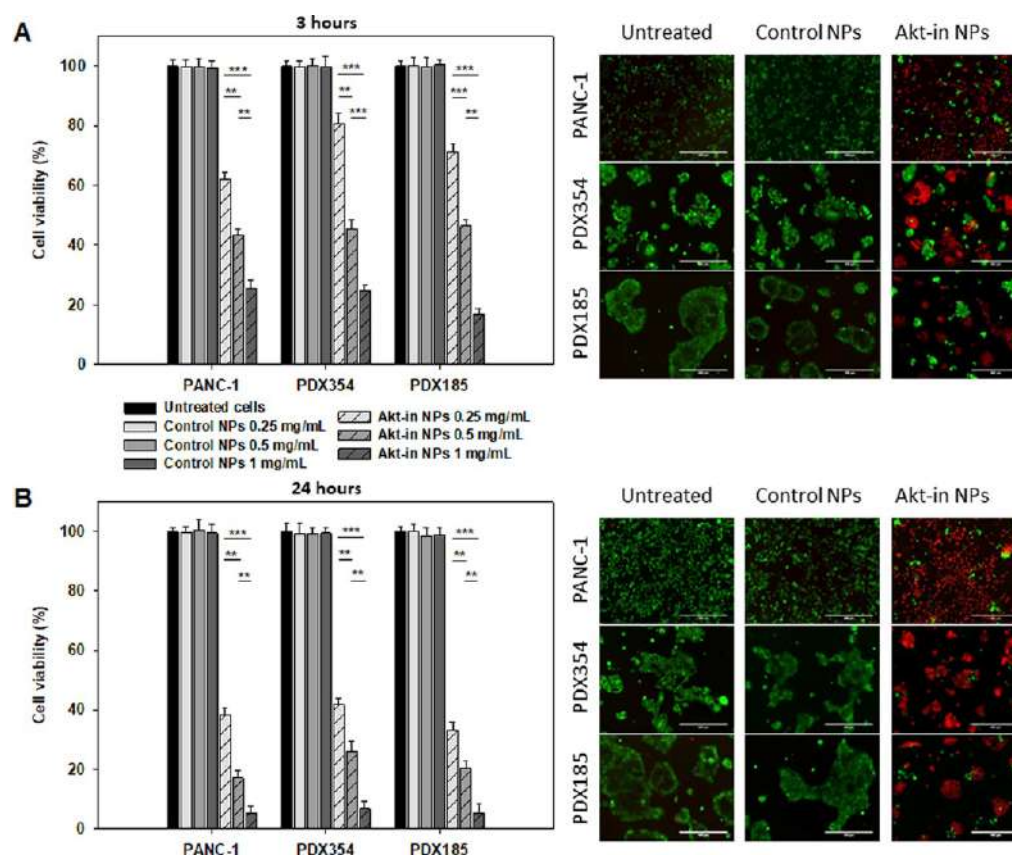


**Figure 4.** Percentage of viability of PANC-1 and patient-derived PDX354 and PDX185 cells compared to untreated cells. Cells were incubated with three concentrations of control and Akt-in nanoparticles for 3 (A) or 24 h (B), and cell viability was measured following treatment with NPs using the LIVE/DEAD assay.  $n = 3$  independent experiments, each in triplicate. Mean  $\pm$  SD.  $**p < 0.01$ ;  $***p < 0.001$ .

previous work from our group demonstrated that control NPs (without the inhibitor) did not affect cell viability and were innocuous for human primary non-cancerous cells, such as fibroblasts, HUVEC endothelial cells, and mesenchymal stem cells, whereas an enhanced antitumoral effect was observed on cancerous cell viability.<sup>35</sup>

One of the main purposes of drug screening consists of the achievement of predictive models. Although *in vitro* cell culture of established cell lines is a useful tool, the lack of cellular heterogeneity is an important disadvantage. Thus, patient-derived models more accurately mirror the tumor heterogeneity, improving the predictability of therapeutic response to treatment and accelerating the development of novel and more effective therapeutic strategies.<sup>44</sup> Moreover, these models retain most of the morphological and molecular features of the original tumor.<sup>45</sup> For these reasons, we tested our drug delivery systems in pancreatic cancer patient-derived cells.

The biological effect of our NPs on the pancreatic cancer cell line PANC-1 and the patient-derived cells PDX185 and PDX354 was determined by evaluating changes in cellular metabolic activity (Figure 3). Cancer cells were incubated for 3 or 24 h with three different concentrations of ELR NPs, ranging from the critical micellar concentration (CMC) 0.25 to 1 mg/mL. As shown in Figure 3, control NPs did not significantly affect the metabolic activity of any of the cells tested compared to untreated cells. Results showed no difference either between the three different NP concentrations or between time points. Thus, we can conclude that the basic ELR structure of our nanocarriers did not have any effect on the overall metabolic activity of the pancreatic models used.

Interestingly, when pancreatic cancer cells were incubated with Akt-in ELR NPs for 3 h, cellular metabolism was affected (see Figure 3A). Metabolic activity was decreased to 58, 74, and 63% when PANC-1, PDX354, and PDX185 cells, respectively, were incubated with the lowest dose of NPs loaded with the Akt inhibitor (0.25 mg/mL). When the NP concentration was increased to 0.5 mg/mL, the metabolic activity of the three cell types dropped to 34–38%. Treatment with the highest NP concentration (1 mg/mL) decreased the metabolic activity to 13–18%. These results not only showed a dose-dependent cytotoxic trend but also a time-dependent mode of action. It also confirmed that any reduction in metabolic activity observed was due to the presence of the Akt inhibitor and not the ELR structure.

As expected, when the incubation time with the Akt-in NPs was increased from 3 to 24 h, the cytotoxic effect was enhanced (Figure 3B). Indeed, the highest NP concentration (1 mg/mL) strongly decreased metabolic activity to 4, 6, and 7% in PANC-1, PDX354, and PDX185, respectively. Regarding the intermediate NP concentration (0.5 mg/mL), the three cell lines showed only 12–14% of metabolic activity. Lastly, when PANC-1, PDX354, and PDX185 cells were treated with the lowest concentration of Akt-in NPs (0.25 mg/mL), cellular metabolism was decreased to 27, 31, and 28%, respectively. Thus, results suggest that our NPs improved the cytotoxic effect of the inhibitor on cancer cells in a time- (8 times faster) and dose-dependent manner (5 times lower concentration), compared to the nude inhibitor.

Once the antitumor effect of Akt-in ELR nanoparticles was validated, we evaluated the percentage of metabolically active

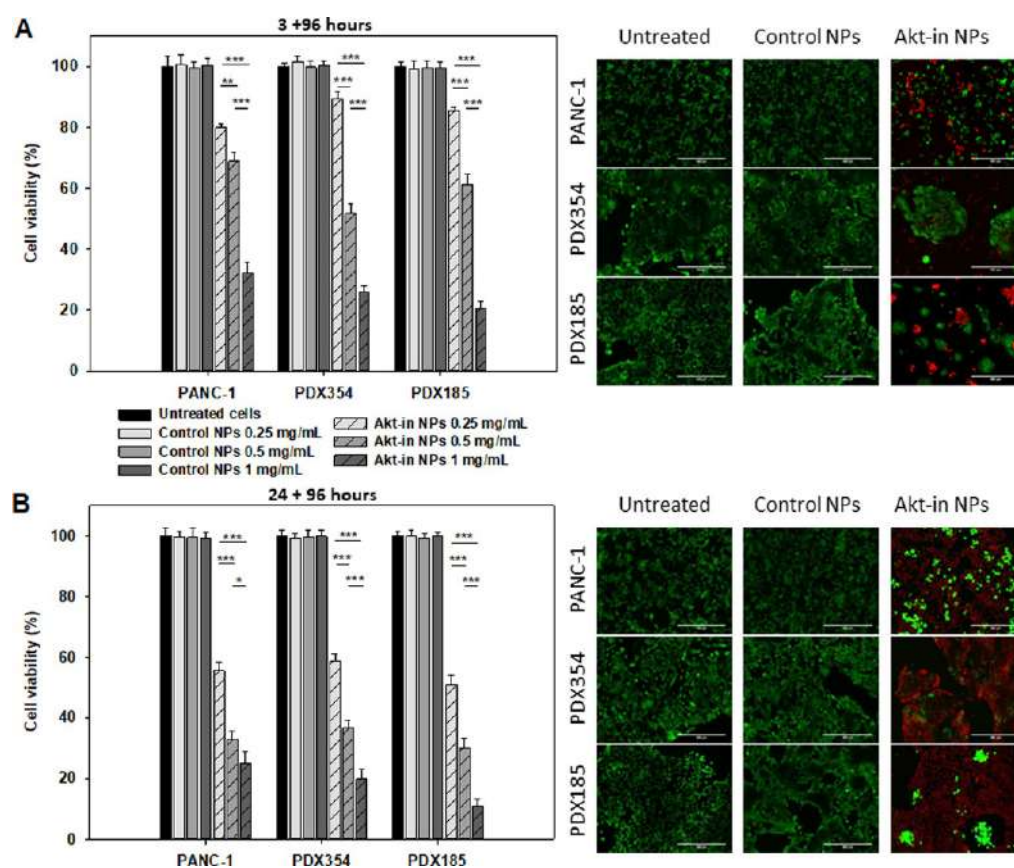


**Figure 5.** Percentage of viability of PANC-1 and patient-derived PDX354 and PDX185 cells compared to untreated cells. Cells were incubated with three concentrations of control and Akt-in nanoparticles for 3 (A) or 24 h (B). Media was refreshed and cell viability 96 h after treatment was measured using the LIVE/DEAD assay kit. Representative fluorescence microscopy images. Scale bars: 100  $\mu\text{m}$ .  $n = 3$  independent experiments, each in triplicate. Mean  $\pm$  SD.  $**p < 0.01$ ;  $***p < 0.001$ .

cells 96 h after the end of the treatments to check for any possible recovery (Figure 3C,D). As previously observed, control NPs did not affect cellular metabolism, confirming their high biocompatibility. Recovery time slightly decreased the effect of Akt-in NPs on metabolic activity, particularly when using the lowest Akt-in NP concentration and only 3 h incubation time. When the highest concentration of Akt-in NPs was used (1 mg/mL), cellular metabolism decreased to 22, 23, and 18% in PANC-1, PDX354, and PDX185 cells, respectively. However, this effect was less significant when cells were incubated for 24 h with 1 mg/mL Akt-in NPs (cellular metabolism rates of 13–19%), which is in line with our previous results. Interestingly, patient-derived cells showed less metabolic recovery than PANC-1 cells when treated with 1 mg/mL NPs due to the increased NPs internalization previously observed.

**2.4. Effect of Nanoparticles on Cell Viability.** Once the effect of the different ELR nanoparticles on the metabolic activity of pancreatic cancer cells was determined, cell viability was analyzed by the differential staining of live and dead cells with specific fluorescent dyes (Figures 4 and 5). For this purpose, pancreatic cancer cells were incubated under the same treatment conditions of previous experiments. First, the cytotoxic effect of control NPs was determined. Control NPs did not significantly affect the viability of any of the three pancreatic cancer cell lines. Indeed, results showed no difference between the three different concentrations tested

at any time point. We can conclude that control NPs were safe and did not induce cell death.

Conversely, when pancreatic cancer cells were incubated with Akt-in NPs, cellular viability was decreased. At a concentration of 0.25 mg/mL, cellular viability was higher than 60% after treating the cells for 3 h with Akt-in NPs, while when using the intermediate concentration, the three cell lines showed 43–47% viability. When the NP dose was increased to 1 mg/mL, PANC-1 cells and PDX354 showed 25% viability, whereas PDX185 cells were more sensitive and only 17% survived.

Furthermore, we observed that cell viability was dependent on the incubation time with therapeutic ELR NPs. When increasing the incubation time from 3 to 24 h, results showed that Akt-in NPs were more effective (Figure 4B), matching the MTT data. At the lowest NP concentration, PANC-1, PDX354, and PDX185 cells showed 38, 42, and 34% cell viability, respectively. As expected, cells treated with the intermediate Akt-in NP concentration (0.5 mg/mL) were more affected showing 18, 26, and 22% cell viability after treatment, for PANC-1, PDX354, and PDX185 cells, respectively. When cells were incubated with the highest Akt-in NPs concentration (1 mg/mL), the three pancreatic cancer cell lines showed similar viability values (4–7%) after treatment. Representative fluorescence microscopy images corroborated the quantitative data obtained.

The effect of ELR NPs on cell viability was also evaluated 96 h after treatment for long-term recovery studies (Figure 5).

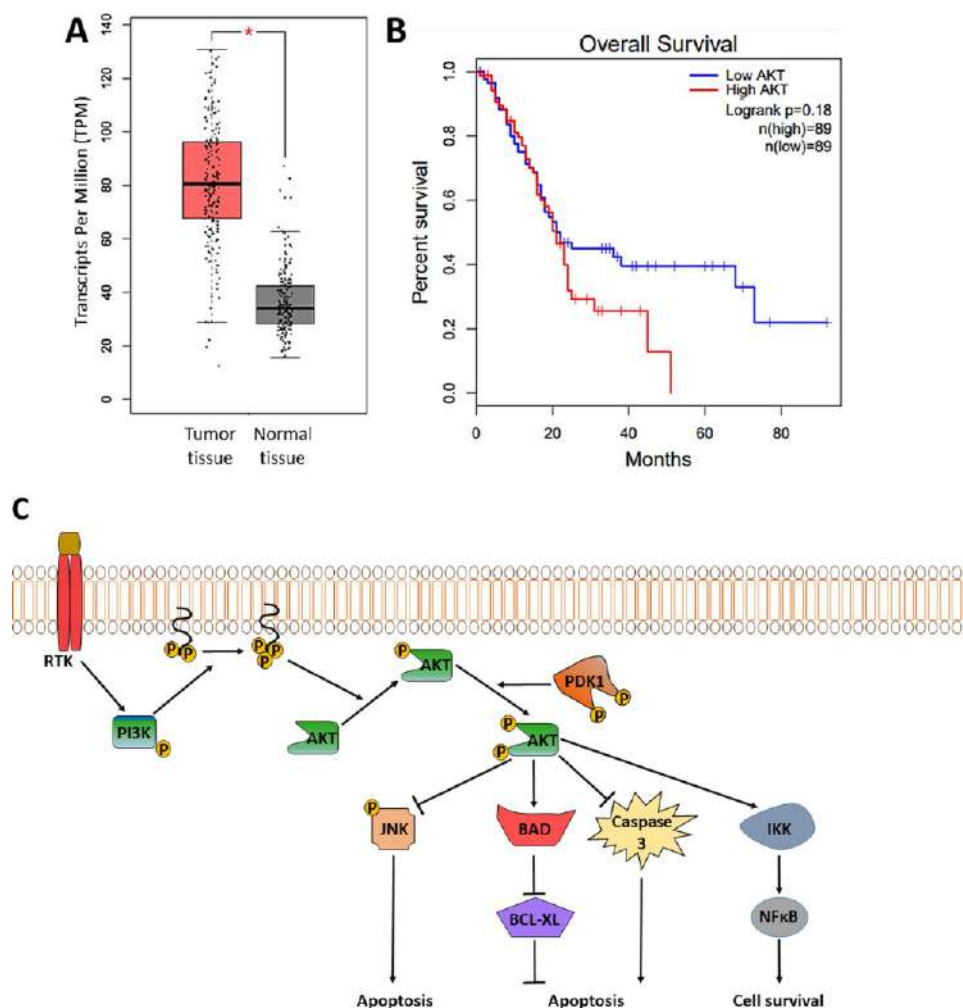


**Figure 6.** (A) Differential expression of Akt in pancreatic tumors and normal tissue. Graph produced using the webserver GEPIA.<sup>46</sup> (B) Kaplan–Meier survival plot for pancreatic cancer where high expression of Akt has significant ( $p < 0.001$ ) association with poor patient survival. Graph produced using the webserver GEPIA.<sup>46</sup> (C) Cell signaling pathways involving Akt kinase. Akt is phosphorylated by PI3K and PDK1. Active Akt kinase plays important roles in multiple signaling pathways regulating apoptosis and cell survival.

Results confirmed that control NPs were completely innocuous and did not affect cell viability, a key parameter when developing novel drug delivery systems. When cells were treated with 0.25 mg/mL Akt-in NPs for 3 h and evaluated 96 h post-treatment, the three pancreatic cancer cell lines showed viability above 80%. When the intermediate dose was used, the recovery effect was lower, except for PANC-1 cells, which showed 67% of cell viability. However, when cancer cells were treated with 1 mg/mL Akt-in NPs, cell recovery was minimal, which corroborated MTT results and validated this concentration as the most effective one.

The percentage of metabolic activity recovery post-treatment was much lower when cells were treated with NPs for 24 h. Cell viability of PANC-1, PDX354, and PDX185 cells did not reach 60% when treated with the lowest dose of ELR NPs (0.25 mg/mL). When cells were treated with the intermediate concentration, pancreatic cancer cells only recovered 10% of their proliferation capacity. A significant recovery was not observed when cells were treated with the highest dose, thereby validating the efficacy of our NPs.

Hence, these results support that Akt inhibition through our advanced NPs is a promising strategy for the treatment of PDAC and opens the possibility to explore dual or multimodal

therapy in combination with chemotherapy to advance clinical translation.

Based on our previous results and with the future goal of developing combination treatment strategies, the intermediate concentration of ELR-based NPs was selected for further experiments, as this dose affected metabolic activity and cell viability in primary pancreatic cancer cells. Moreover, a previous work determined that a dose of 0.5 mg/mL markedly affected breast and colorectal cancer cells viability without significant effects in primary non-cancerous cells, such as fibroblasts, endothelial, and mesenchymal stem cells.<sup>35</sup>

**2.5. Effect of Nanoparticles on Cell Morphology.** After determining the effect of ELRs NPs on cell viability, proliferation, and metabolic activity, cell morphology was also studied to corroborate how pancreatic cancer cells were affected by the treatment with our smart nanocarriers (Figure S6). PANC-1, PDX185, and PDX354 cells were incubated with 0.5 mg/mL ELR NPs for 3 and 24 h, and cell morphology was evaluated.

No major differences in cellular morphology and cell density were observed in any of the three lines incubated with control NPs compared to untreated controls, at any of the selected incubation times. PANC-1 cells (Figure S6A) showed a higher

sensitivity to the 3 h treatment with NPs containing the inhibitor than PDXs, corroborating the data obtained by MTT and LIVE/DEAD assays. Treatments for 24 h with Akt-in NPs showed a complete disruption of the normal pattern of growth and colony formation capacity of the three cell types. The few surviving cells after 24 h of treatment displayed a round morphology typical of cells undergoing cell death, which strongly supports the higher effect of Akt-in NPs in cell viability previously observed.

In experimental conditions where cells were treated for 3 or 24 h and then media was refreshed to allow for any possible recovery during the next 96 h, all three cell types showed a strong decrease in cell density, suggesting no major cell recovery after treatment.

**2.6. Action of Akt Inhibition on Cell Signaling Pathways.** The primary aim of this work was to achieve a controlled delivery of the small peptide inhibitor of the phosphorylation of Akt to the cellular cytoplasm. In this regard, the expression of proteins involved in cell signaling pathways controlled by Akt was studied to confirm the NPs mechanism of action and their accurate effect in Akt phosphorylation.

Akt protein, once phosphorylated at the threonine and serine residues, becomes active and plays a key role in multiple cell signaling pathways summarized in Figure 6. Thus, Akt kinase controls cell growth, proliferation, and survival<sup>22,23</sup> and its higher expression correlates with poor prognosis and lower survival rates in pancreatic cancer patients (Figure 6),<sup>46</sup> thereby making Akt a promising target for cancer therapy.

Immunoblots were performed to check the mechanism of action of the inhibitor released from the NPs. Expression levels of several proteins involved in cell signaling pathways regulated by Akt were evaluated (Figure 7). Pancreatic tumor cells showed serine 473 phosphorylated Akt kinase, corroborating that cancer cells often have this signaling pathway constitutively activated. Remarkably, when cancerous cells were treated with control NPs, the phosphorylation of Akt protein was not altered after 3 (Figure 7A) or 24 h (Figure 7B). However, Akt phosphorylation was markedly inhibited when cells were incubated with Akt-in NPs after both incubation times. Furthermore, expression levels of total Akt protein did not change after treatment with control NPs or Akt-in NPs.

Even though the blockade of Akt phosphorylation and activation was demonstrated, we also measured the downstream effect of inhibiting Akt in pancreatic cancer cells. Nuclear factor kappa-B, NF- $\kappa$ B transcription factor, is located downstream in the Akt signaling pathway and is activated by phosphorylated Akt kinase (Figure 6).<sup>47</sup> Since NF- $\kappa$ B protein regulates cell survival, a key hallmark of cancer cells, NF- $\kappa$ B expression levels were measured.<sup>48</sup> Figure 7 shows untreated pancreatic cancer cells displaying a high expression of NF- $\kappa$ B. These expression levels were not altered when PANC-1 and patient-derived pancreatic cancer cells were treated with control NPs. In contrast, when cells were incubated with ELRs NPs carrying the Akt inhibitor for 3 (Figure 7A) or 24 h (Figure 7B), expression levels of NF- $\kappa$ B decreased. These results corroborated that Akt phosphorylation, and consequent activation and signaling, was properly inhibited, and cell survival controlled by NF- $\kappa$ B was also blocked by treating the cells with our Akt-in loaded NPs.

In a previous work, we demonstrated that breast and colorectal cancer cells underwent apoptosis after treatment

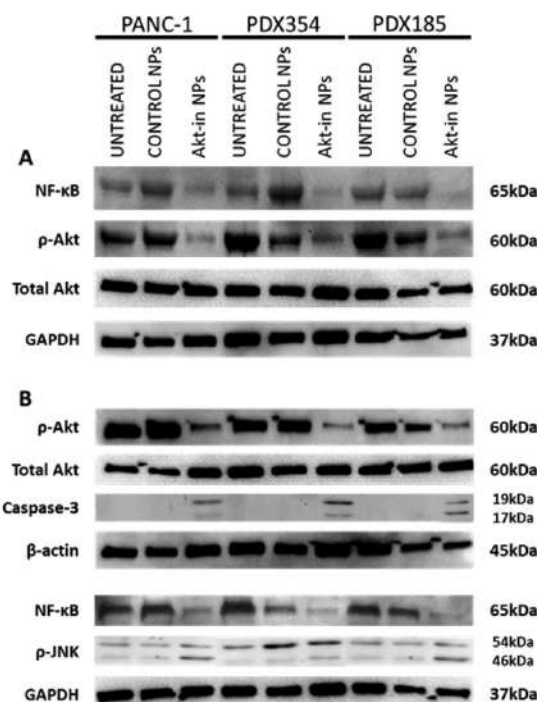


**Figure 7.** Effect of ELR nanoparticles on cell signaling pathways involving Akt kinase. PANC-1, PDX354, and PDX185 cells were incubated with 0.5 mg/mL control or Akt-in nanoparticles for 3 (A) or 24 h (B). Immunoblots were performed to measure expression levels of NF- $\kappa$ B, Akt phosphorylation at Ser473, total Akt, cleaved caspase-3, and p-JNK. Glyceraldehyde 3-phosphate dehydrogenase (GAPDH) and  $\beta$ -actin were used as loading controls.  $n = 3$  independent experiments.

with Akt-in NPs.<sup>35</sup> We hypothesized that when NPs were able to inhibit the anti-apoptotic effect of Akt activation, cancerous cells would undergo apoptosis-mediated death. For this reason, cleaved caspase 3 expression levels were evaluated in our pancreatic models as this protein plays a key role in apoptosis.<sup>49</sup> Cleaved caspase 3 was not detected 3 h after treatment with NPs carrying the Akt inhibitor (data not shown); however, it was detected 24 h after treatment (Figure 7B). Results proved that untreated cells, which possessed aberrant growth, showed no cleaved caspase 3 expression. When pancreatic cancer cells were incubated with control NPs, active caspase 3 expression was not increased. These results validate that control NPs were completely innocuous for the cells. Thus, we could conclude that effective inhibition of Akt phosphorylation and activation allowed pancreatic cancer cells to undergo apoptosis-mediated death.

Moreover, phosphorylation levels of the JNK protein were determined after 24 h of incubation with ELR-based NPs (Figure 7B), as this pro-apoptotic protein is inhibited by phosphorylated Akt kinase in cancer cells (Figure 6).<sup>50,51</sup> Results showed that phosphorylation and consequent activation of JNK protein was not altered by the treatment with control NPs. However, enhanced phosphorylation levels of JNK protein were detected when the activation of Akt kinase was inhibited by ELRs NPs carrying the small inhibitor. These results demonstrated that the accurate mode of action of our NPs over Akt protein was not only due to the inhibition of its phosphorylation but also due to the blockade of cell survival signaling controlled by the NF- $\kappa$ B pathway and the subsequent

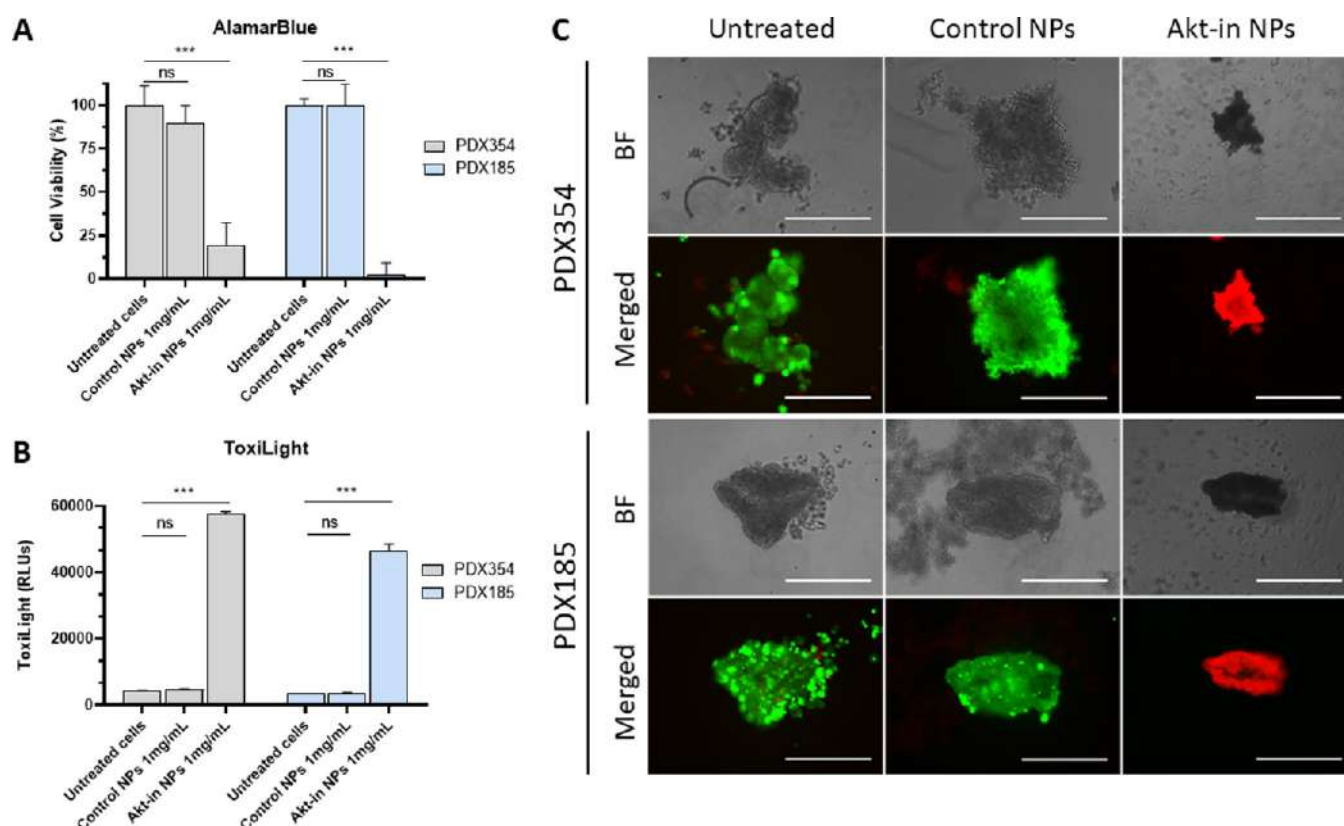


**Figure 8.** Treatment of PDX-derived 3D cultures with ELR NPs. PDX354 or PDX185 spheroids were treated for 24 h with 1 mg/mL Akt-in NPs or control-NPs. Untreated spheroids were used for comparison. (A) Percentage of cell viability at 0 h after treatment compared to untreated controls, using the AlamarBlue assay. (B) Viability ToxiLight assay at 0 h after treatment. (C) Representative images of PDX-derived spheroids treated with NPs as indicated and stained with the LIVE/DEAD cytotoxicity assay. Green fluorescence (calcein-AM) represents live cells with an intact cell membrane, and red fluorescence (EthD-1) indicates dead cells. Bright field images were taken for comparison. Scale bars: 400  $\mu\text{m}$ .  $n = 3$  independent experiments, 6 spheroids per treatment group. Mean  $\pm$  SD. \*\*\* $p < 0.001$ , ns = not significant.

activation of the  $\rho$ -JNK pathway leading to caspase 3-mediated cell apoptosis.

**2.7. Validation of Treatment Efficacy in Patient-Derived 3D Cultures.** Based on the promising results obtained in 2D experiments, 24 h incubation and 1 mg/mL Akt-in NPs were the optimal incubation time and NP dose for validation in patient-derived spheroids before moving to *in vivo* testing. The use of clinically relevant 3D models, which better mimic the biology of human tumors, can accelerate the translatability of our smart nanodevices. PDX spheroids were treated at day 3 after seeding based on previous studies by our group showing a spheroid diameter below 500  $\mu\text{m}$ .

As shown in Figure 8A, treatment with 1 mg/mL control NPs did not significantly affect the metabolic activity of PDX354 or PDX185-derived spheroids, as assessed by the AlamarBlue assay, showing similar values to untreated spheroids. However, treatment with 1 mg/mL Akt-in NPs drastically reduced metabolic activity to 19% (PDX354) or 2% (PDX185), corroborating 2D cultures MTT data. Cell viability of the spheroids was also analyzed after treatment, using the ToxiLight assay (Figure 8B), which measures the release of the enzyme adenylate kinase from cells with compromised cell membrane integrity and, therefore, undergoing cell death. PDX354 spheroids treated with control NPs showed similar values to untreated controls, whereas spheroids treated with Akt-in NPs showed a 13-fold increase in luminescence values. Similar results were obtained with PDX185 spheroids, which

showed a 10-fold increased cell death after the Akt-in NP treatment.

Moreover, LIVE/DEAD assays were performed in treated and untreated PDX-derived spheroids to further confirm ToxiLight viability data. Figure 8C shows representative images of spheroids after treatment. Spheroids treated with control NPs showed the totality of cells forming the 3D models alive (bright green fluorescence), similar to untreated controls. Conversely, spheroids treated with 1 mg/mL Akt-in NPs showed a high increase in cell death marked by red fluorescence and no detectable green fluorescence (live cells), validating the therapeutic efficacy of our Akt-in NPs.

**2.8. *In Vivo* Pharmacokinetic Profile of ELR-Based Nanoparticles.** Short circulating half-life is the main disadvantage of therapeutic agents, such as chemotherapeutic drugs or peptides. This requires repeated administration of high concentrations to obtain therapeutically effective levels, which usually result in high toxicity and off-target effects in healthy tissues.<sup>52</sup> Therapeutic molecules need to overcome several biological barriers to reach the target tissue and ensure an effective dose. ELR-based carriers play an interesting role overcoming all these limitations as they are able to extend the circulating half-life of therapeutic peptides or drugs and also improve their specific accumulation and pharmacokinetics.<sup>10</sup>

The pharmacokinetic profiles of control and Akt-in NPs were compared after intravenous administration of fluorescein-labeled ELRs in BALB/c mice and collection of blood samples at various time points. Figure S7 shows the plasma

concentration versus time curve for both ELR polymers. A one-phase decay behavior was observed. Therefore, the one-compartment model was used to fit the plasma concentration–time curve. This model assumes that the whole body acts like a single uniform compartment, the drug is distributed instantaneously throughout the entire body, and drug elimination occurs immediately after the intravenous bolus injection.<sup>53,54</sup>

Pharmacokinetic parameters are shown in Table 2. The distribution volume of control and Akt-in NPs was almost the

**Table 2. Pharmacokinetic Parameters of Intravenously Administered Control and Akt-in Nanoparticles in Mice ( $n = 5$  per Treatment Group)<sup>a</sup>**

	control NPs	Akt-in NPs
AUC ( $\mu\text{m}\cdot\text{h}$ )	148 $\pm$ 8	129 $\pm$ 12
F (%)	100	100
CL (mL·h)	0.22 $\pm$ 0.08	0.25 $\pm$ 0.04
Vd (mL)	1.8 $\pm$ 0.3	1.9 $\pm$ 0.5
$T_{1/2}$ elimination (h)	5.8 $\pm$ 0.4	5.3 $\pm$ 0.6
$K_{\text{elimination}}$ ( $\text{h}^{-1}$ )	0.12 $\pm$ 0.02	0.13 $\pm$ 0.02

<sup>a</sup>One compartment analysis. Mean  $\pm$  SD. Abbreviations: AUC: area under the curve, F: bioavailability, CL: clearance, Vd: volume of distribution,  $T_{1/2}$  elimination: terminal half-life,  $K_{\text{elimination}}$ : elimination rate constant.

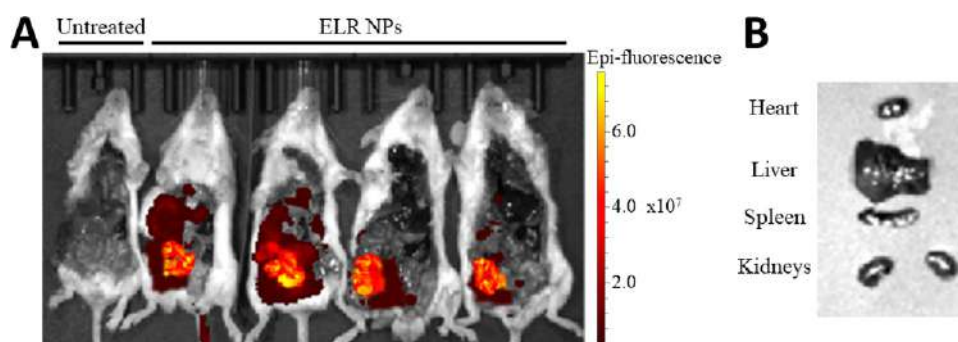
same as the blood volume of a mouse. These values indicate that NPs were not rapidly accumulated in organs and tissues after administration. As presented in Table 2, ELR-based NPs showed long half-life (5.8 and 5.3 h for control and Akt-in NPs, respectively), similar to previous ELRs developed for drug delivery purposes.<sup>55,56</sup> Moreover, no statistical difference was observed in any parameter when comparing control and Akt-in NPs, which indicates that both NPs have similar *in vivo* distribution and elimination profiles. These pharmacokinetic parameters are considered suitable features in terms of delivery of therapeutic agents and drugs.<sup>53,55</sup> These results indicate that our advanced NPs are suitable biomaterials for drug delivery purposes and future drug response studies.

**2.9. In Vivo Biodistribution.** The pharmacokinetic profile of ELR-based NPs showed that our nanocarriers could be a suitable device for drug delivery purposes presenting appropriate distribution volume and half-life. For this reason, the *in vivo* biodistribution of our NPs was also evaluated

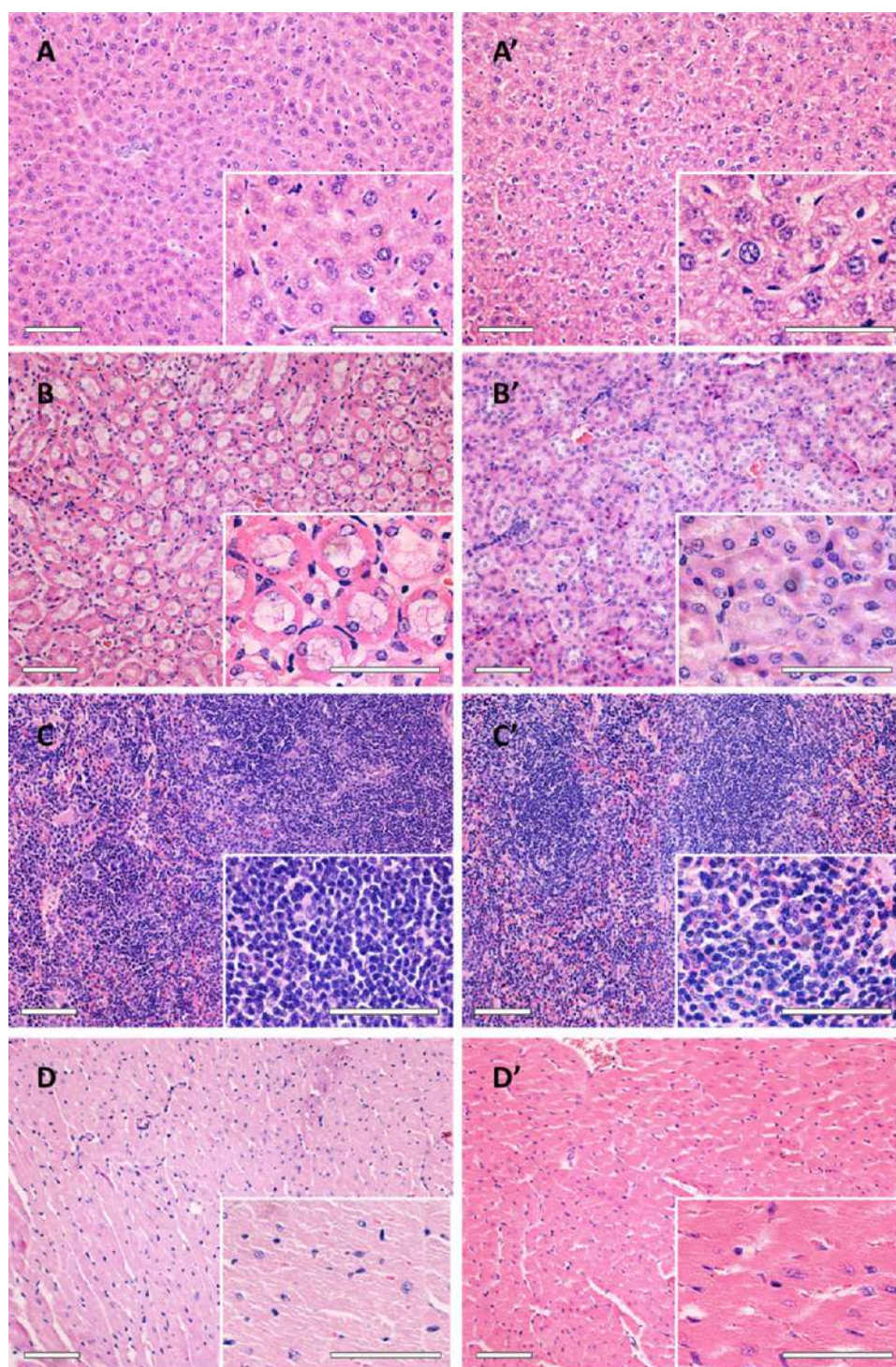
(Figure 9) to determine whether the NPs get preferentially accumulated in any specific organ upon intravenous administration. Cy5-labeled NPs were injected intravenously into BALB/c mice, and the biodistribution was monitored using the IVIS *in vivo* imaging system after subtracting background from an untreated mouse. Moreover, the heart, spleen, liver, and kidneys were collected and scanned.

Figure 9A shows an increased accumulation of NPs in the gastrointestinal tract (GIT) 6 h post injection. GIT has been proposed as one of the major organs for nanomaterials interaction and uptake.<sup>57,58</sup> Thus, several GIT features play a role in this, such as the presence of enterocytes or the mucus layer.<sup>59,60</sup> Moreover, intestinal mucus secretion enhances nanomedicine transportation and uptake by endocytosis-mediated pathways.<sup>61</sup> One of the main problems of NPs for drug delivery purposes is their accumulation in critical organs such as the heart, liver, or kidneys. NPs bigger than 100 nm are not able to escape from liver capture.<sup>62</sup> Also, particles smaller than 10 nm suffer from renal clearance.<sup>15</sup> Therefore, NPs with sizes ranging from 10 to 100 nm are preferred.<sup>63</sup> In this work, our ELR-based NPs showed sizes of 67.1  $\pm$  2.5 and 73.1  $\pm$  3.2 nm for control and Akt-in, respectively. Thus, our NPs should not be excreted through the kidneys, and due to the protein and biodegradable nature of the ELR scaffold, the NPs are expected to be degraded in the medium/long term. Remarkably, there was no signal detected in the liver or kidneys (Figure 9B). Furthermore, there was no heart accumulation (Figure 9B). This is important, as some of the side effects of current chemotherapeutic drugs are due to cardiac toxicity.<sup>64</sup> In this context, we could conclude that the developed NPs are suitable drug delivery nanosystems because no accumulation was appreciated in critical organs 6 h after injection.

**2.10. Histopathology Examination of Liver, Kidney, Heart, and Spleen.** The pharmacokinetic profile and organ biodistribution of our ELR-based nanocarriers confirmed their potential safety as no critical accumulation was observed in key organs. An analysis of the organ microstructure was also performed to check for any internal damage that may have arisen upon injection of control and Akt-in NPs. In this regard, sections from key organs including the liver, kidney, spleen, and heart were stained with H&E (Figure 10) and assessed on key parameters of the organ microstructure and physiology, such as (i) liver: steatosis, lobular inflammation, ballooning,



**Figure 9.** *In vivo* imaging of the biodistribution of Cy5-labeled NPs into BALB/c mice. Cy-5 labeled ELR nanoparticles were systemically injected via tail vein. After 6 h, animals were sacrificed and transferred immediately to the IVIS imaging system. (A) The untreated animal (first from left) was measured as control. The other four animals were injected intravenously with 5 mg/Kg Cy5-labeled NPs via tail vein. (B) Heart, liver, spleen, and kidneys from treated animals were collected, and their fluorescence was scanned to determine the possible accumulation of nanoparticles within these organs.



**Figure 10.** Histological evaluation after injection of nanoparticles. Selected organs from BALB/c mice treated with control (A–D) or Akt-in NPs (A'–D'). (A) Liver; (B) kidney; (C) spleen; and (D) heart. Scale bars: 50  $\mu\text{m}$ .

fibrosis, and portal inflammation; (ii) spleen: neutrophils, necrosis and thrombosis; (iii) heart: heart myocardial damage; and (iv) kidneys: glomerular cellularity, tubular vacuolation, interstitial inflammation, interstitial fibrosis, and vessels. Liver assessment was based on non-alcoholic fatty liver disease (NAFLD) activity score (NAS) type scoring.<sup>65</sup> Spleen assessment was based on the methodology described by Gibson-Corley *et al.*,<sup>66</sup> and the heart score was based on a system developed by Sachdeva *et al.*<sup>67</sup> The results obtained

from the examination did not show significant differences, and only minor abnormalities were observed in organs of mice treated with control or Akt-in NPs, thereby highlighting the safety and tolerability of our nanocarriers as drug delivery systems (Figure 10).

This is the first time that the safety of the nanocarriers was determined, and results showed that NPs did not generate major deterioration in organs typically affected by free or encapsulated drugs. In addition, it was confirmed that the

incorporation of the Akt inhibitor to the nanoconstructs did not change the mode of action of the nanomedicine compared to its analogous control NPs.

### 3. CONCLUSIONS

Low specificity, off-target side effects and poor drug accumulation in the target site due to the difficult access to the tumor, particularly in desmoplastic lesions such as pancreatic cancer, are major hurdles in cancer therapy leading to limited success of current drugs. Nanotechnology appears as a promising approach for controlled drug delivery and optimal-dose reduction of therapeutic drugs.

In this work, we took advantage of ELR polymers to create advanced NPs with high conformational complexity for controlled drug delivery. The  $73.1 \pm 3.2$  nm NPs carried a small 15 amino acid peptide, which bound to the cytoplasmic Akt protein inhibiting its activation, as well as different bioactive sequences to facilitate their internalization, the enzymatic release of the inhibitor and the escape from the endo/lysosomes to the cellular cytoplasm to reach its target.

The NP anti-tumor activity and mechanism of action was evaluated for the first time in clinically relevant pancreatic cancer patient-derived models. Our results showed that both control and Akt-in NPs were internalized and accumulated within the lysosomes of pancreatic cancer cells, where the escape sequences were designed to release the inhibitor to the cytoplasm. In addition, results demonstrated that Akt-in NPs not only reduced cellular metabolic activity but also cell viability. In fact, cancer cells underwent apoptosis. Contrarily, control NPs did not impact cell metabolism nor viability. Based on our results, we can conclude that our NPs inhibited the Akt signaling pathway and, consequently, blocked cell survival controlled by the NF- $\kappa$ B pathway. To increase the translatability of these findings, we validated the therapeutic efficacy of our Akt-in NPs in clinically relevant 3D models (spheroids), which better mimic the complexity and aggressiveness of PDAC tumors than 2D cell cultures. Thus, these smart NPs were shown to be an accurate and promising drug delivery system for controlled release in pancreatic cancer cells, including 3D models.

*In vivo* pharmacokinetic profiling showed that both control and Akt-in NPs have long half-lives and proper distribution volumes, which suggested that they are suitable drug delivery devices for systemic administration. Furthermore, *in vivo* assays showed that the NPs did not accumulate in critical organs, damage their microstructure or alter their normal physiology, some of the most common disadvantages leading to low accuracy and undesired side effects.

To the best of our knowledge, this is the first time that NPs carrying an Akt inhibitor have been evaluated for therapeutic purposes in pancreatic cancer patient-derived models. As Akt protein is not only overexpressed in pancreatic but also in other multiple types of cancer, different studies could be potentially accomplished to test the efficacy of this nanodevice in other cancer models. Even though we studied the accuracy of these NPs in clinically relevant patient-derived models, further studies are needed to determine the effectiveness of these NPs *in vivo* before moving into clinical trials. Thus, a dual combination approach could be explored involving both self-assembling NPs encapsulating our Akt inhibitor and chemotherapy. In the future, cancer patients overexpressing the Akt protein may be good candidates for clinical studies with NPs

carrying an Akt inhibitor, which could improve the problems caused by current unspecific chemotherapeutic drugs.

### 4. MATERIALS AND METHODS

**4.1. Chemical Reagents and Cell Lines.** The LIVE/DEAD viability/cytotoxicity kit for mammalian cells, LysoTracker Red DND-99, and AlamarBlue were supplied by Invitrogen. Thiazolyl blue tetrazolium bromide (MTT), anhydrous *N,N*-dimethylformamide (DMF), dimethyl sulfoxide (DMSO), methanol, and DMEM media (Dulbecco's Modified Eagle's Medium) were purchased from Sigma-Aldrich. Fetal bovine serum (FBS), penicillin/streptomycin, RPMI media (Roswell Park Memorial Institute), Trypsin-EDTA, and phosphate buffered saline (PBS) were supplied by Gibco. NHS-Fluorescein and NHS-Cy5 were provided by Lumiprobe. The ToxiLight assay was supplied by Lonza. DePex mounting medium was purchased from Serva. The Cell lysis RIPA buffer and Bradford reagent were supplied by BIORAD. The PhosSTOP phosphatase inhibitor cocktail and COMPLETE protease inhibitor cocktail were purchased from Roche. Primary antibodies against total Akt (#9272),  $\rho$ -Akt Ser473 (#9271),  $\rho$ -JNK (#9251), NF- $\kappa$ B p65 (#4764), cleaved caspase-3 Asp175 (#9661),  $\beta$ -actin (#3700), and GAPDH (sc-32,233) were purchased from Cell Signalling and Santa Cruz Biotechnology. Goat secondary antibodies against rabbit (P0448) and mouse (P0447) were supplied by Dako. The Western-Ready ECL Substrate kit was supplied by BioLegend. Isoflurane was purchased from Esteve. Harris Haematoxylin and Eosin were purchased from Leica.

Human pancreatic cancer cells PANC-1 (ATCC CRL-1469) were purchased from the American Type Culture Collection (ATCC). Pancreatic adenocarcinoma patient-derived xenograft models (PDXs) 354 and 185 were obtained from the Biobank of the Spanish National Cancer Research Centre (CNIO), Madrid, Spain (references B18230PDX7, B18243PDX4). Cells were isolated from these tumors and established for *in vitro* culture as described elsewhere.<sup>68</sup>

**4.2. ELR Design, Bioproduction, and Purification.** The ELRs used in this work were obtained as previously described.<sup>35,69</sup> The construction of the final fusion genes with fully controlled chain composition and length was carried out by sequential introduction of the monomer genes by using the recursive directional ligation method (RDL). The expression vectors containing the desired ELR genes were transformed into the *Escherichia coli* BLR (DE3) strain and bioproduced in a 15 L bioreactor (Applikon Biotechnology). The ELRs were purified by several cooling and heating purification cycles (Inverse Transition Cycling-ITC), and additional NaCl and NaOH treatments were performed in order to remove endotoxins.<sup>70</sup> Finally, the product was dialyzed against ultrapure water type I, sterilized by filtration (0.22  $\mu$ m filters, Nalgene), and freeze-dried prior to storage. Sodium dodecyl sulfate polyacrylamide gel electrophoresis (SDS-PAGE) and mass spectrometry (MALDI-TOF/MS) were performed to determine the molecular weight and purity of the recombinamers. High performance liquid chromatography (HPLC) and nuclear magnetic resonance (NMR) were carried out by Laboratory of Instrumental Technics from University of Valladolid to verify the amino acid composition. The Endosafe-PTSTM test was used in order to measure endotoxin levels (Charles River).

**4.3. Physicochemical Characterization.** Transition temperatures were determined by differential scanning calorimetry (DSC) using a Mettler Toledo 822e with a liquid nitrogen cooler. An indium standard was used for calibration of temperature and enthalpy. ELR samples were prepared in PBS (pH 7.4) at 50 mg/mL. A total of 20  $\mu$ L aliquot of sample and the corresponding PBS reference were subjected first to an isothermal stage (5 min at 0 °C to stabilize the temperature and state of the samples) and then heated from 0 to 60 °C at 5 °C/min. For enthalpy values, endothermic processes were taken as negative and exothermic processes as positive.

The particle size and  $\zeta$ -potential of the polymers were determined by dynamic light scattering (DLS) using a Zetasizer Nano ZS (Malvern Instruments Ltd.) at 37 °C. Samples were prepared by dissolving the ELRs in PBS (pH 7.4) or ultrapure water type I (pH

7.4) when indicated. Samples were stored overnight at 4 °C in order to allow complete dissolution and filtered using a 0.45  $\mu\text{m}$  poly(vinylidene difluoride) (PVDF) syringe filter. Samples were incubated at 37 °C for 30 min in order to allow self-assembling and then introduced into polystyrene cuvettes. Then, samples were stabilized for 2 min at the desired temperature before the measurements. Autocorrelation functions were used to obtain the size distribution and polydispersity index (PDI). Z-average mean (nm) and  $\zeta$ -potential (mV) were used for data analysis. Three different samples were analyzed for statistical purposes.

**4.4. Fluorescent ELR Labeling.** ELR polymers were covalently modified with NHS-Fluorescein or NHS-Cy5 by conjugation to free amines, when indicated. NHS-Fluorescein or NHS-Cy5 was dissolved in DMF at 10 mg/mL. Three equivalents of fluorophore were added to ELR polymers dissolved in DMF and incubated at 4 °C for 2 h. Finally, the polymer was dialyzed against ultrapure water type I in order to discard solvent and non-conjugated fluorophore and freeze-dried prior to storage.

**4.5. Cell Culture.** Human pancreatic cancer cells PANC-1 (ATCC CRL-1469) were cultured in DMEM media (Dulbecco's Modified Eagle's Medium). PDX-derived cells were cultured in RPMI media (Roswell Park Memorial Institute). Both cell culture media were supplemented with 10% fetal bovine serum (FBS), 100 U/mL penicillin, and 0.1 mg/mL streptomycin. Cells were grown in 75  $\text{cm}^2$  tissue culture flasks (TPP) at 37 °C in 95% humidity and 5%  $\text{CO}_2$ , and once 70–80% confluence was reached, they were either sub-cultured or seeded for the below described protocols. When required, cells were detached using a solution of 0.05% Trypsin–EDTA.

For the spheroid culture, PDX354 and PDX185 cells were seeded on ultra-low attachment (ULA) 96-well plates at  $5 \times 10^3$  cells/well (200  $\mu\text{L}$ /well) in RPMI complete media. ULA plates were pre-coated with a covalently bound hydrophilic polymer that prevents cell attachment promoting cell–cell interactions and thus, spheroid formation. After seeding, ULA plates were centrifuged at  $100 \times g$  for 4 min. Spheroid cultures were maintained in the incubator at 37 °C in 95% humidity and 5%  $\text{CO}_2$ , and 150  $\mu\text{L}$ /well of media was replaced by fresh media every 2 days.

**4.6. Internalization Kinetics.** PANC-1, PDX185 and PDX354 cells ( $5 \times 10^5$  cells/well in 6-well plates) were incubated with complete media containing Cy5-labeled ELR-nanoparticles at 0.5 mg/mL for 3 or 24 h. Cells were washed three times with PBS, trypsinized, and centrifuged for 10 s at  $16800 \times g$ . The supernatant was discarded, and the cell pellet was resuspended in PBS. Samples were measured in a BD LSRII flow cytometer (BD Bioscience) with a laser line at 640 nm (red) and complemented with appropriate filters. 10,000 events per sample were recorded, and single cells were discriminated from doublets by pulse-processing. The FlowJo v10 software (BD Bioscience) was used to analyze and plot the acquired data. Three independent experiments, each in triplicate, were performed.

**4.7. Subcellular Localization.** PANC-1 cells were seeded on FluoroDish glass bottom dishes (World Precision Instruments) at a density of  $8 \times 10^3$  and allowed to attach overnight prior to treatment. Cells were treated with fluorescein-labeled ELR nanoparticles at 0.5 mg/mL for 3 or 24 h. After washing with PBS, cells were incubated with a 75 nM LysoTracker Red DND-99 (1 mM working solution in DMSO) for 1 h at 37 °C. Fluorescence images were taken with an Olympus TIRF confocal microscope equipped with an SIM scanner and an incubator to maintain the conditions constant at 37 °C, 95% humidity, and 5%  $\text{CO}_2$ .

**4.8. Metabolic Activity.** PANC-1 ( $5 \times 10^3$  cells/well) and PDX cells ( $1 \times 10^4$  cells/well) were seeded onto 96-well plates and treated with three different concentrations of ELR nanoparticles (0.25, 0.5 and 1 mg/mL) for 3 and 24 h. Following treatment, the MTT assay was performed according to manufacturer's instructions. Briefly, an MTT stock solution (0.5 mg/mL) was diluted in complete media and filtered using a 0.45  $\mu\text{m}$  PVDF syringe filter. A total of 100  $\mu\text{L}$ /well of MTT solution was added, and samples were incubated for 1 h in the dark. After that, media was removed and 100  $\mu\text{L}$ /well of DMSO was added to dissolve MTT crystals. Absorbance was measured at 562 nm

using an Infinite M200 PRO microplate reader (Tecan Group Ltd.). Additionally, images of cultures were taken with an EVOS digital color fluorescence microscope (Fisher Scientific). Three independent experiments, each in triplicate, were performed.

Metabolic activity of the spheroid cultures was measured using the AlamarBlue assay according to manufacturer's specifications. In short, after treatment, 100  $\mu\text{L}$  of media per well were removed and replaced with 100  $\mu\text{L}$  of a 1:5 dilution of AlamarBlue in complete media. Spheroids were incubated for 24 h with the solution, and after that, the fluorescence at 590 nm of an aliquot of 100  $\mu\text{L}$  of cell supernatant was measured with an Infinite M200 PRO microplate reader. Three independent experiments were performed, with six spheroids per treatment group.

**4.9. Cell Viability and Morphology.** PANC-1, PDX185, and PDX354 cells were seeded and treated as described above for MTT assays. The LIVE/DEAD viability/cytotoxicity assay kit was used according to the manufacturer's instructions. Briefly, cells were incubated with 100  $\mu\text{L}$ /well of a solution containing 1  $\mu\text{M}$  calcein AM and 2  $\mu\text{M}$  EthD-1 (2D cultures) or 4  $\mu\text{M}$  calcein AM and 10  $\mu\text{M}$  EthD-1 for 3D spheroids in DPBS for 20 min in the dark and fluorescence intensity emission was measured at 525 and 645 nm upon excitation at 485 and 525 nm using an Infinite M200 PRO microplate reader. Additionally, images of cultures were taken with an EVOS digital color fluorescence microscope. Three independent experiments, each in triplicate, were performed.

For studies involving 3D spheroids, cytotoxicity was evaluated by ToxiLight. The ToxiLight assay is a bioluminescent non-cytotoxic assay that measures the release of the enzyme adenylate kinase from dying cells, and can be used as a measure of cell viability after treatment. PDX354 and PDX185 spheroid cultures were treated at day 3 for 24 h with 1 mg/mL control or Akt-in NPs. Untreated spheroids were used as controls for comparison. After treatment, a 20  $\mu\text{L}$  aliquot of cell supernatant was used to perform the assay following manufacturer's instructions. Luminescence was measured using an Infinite M200 PRO microplate reader. Three independent experiments were performed, with six spheroids per treatment group.

**4.10. Western Blot.** PANC-1, PDX185, and PDX354 cells ( $5 \times 10^5$  cells/well in 6-well plates) were incubated with complete media containing 0.5 mg/mL nanoparticles for 3 or 24 h. After washing with PBS, cells were lysed with RIPA buffer supplemented with PhosSTOP phosphatase inhibitor cocktail and COMPLETE protease inhibitor cocktail, and protein concentration was measured by the Bradford assay. A total of 50  $\mu\text{g}$  of total protein was separated by standard SDS-PAGE and transferred to PVDF membranes. Blocking was performed with 5% BSA in PBS for 1 h at room temperature. Primary antibodies against total Akt, phosphorylated Akt ( $p$ -Akt), phosphorylated c-Jun N-terminal kinase ( $p$ -JNK), nuclear factor kappa-light-chain-enhancer of activated B cells (NF- $\kappa\text{B}$  p65), cleaved caspase-3,  $\beta$ -actin, and glyceraldehyde 3-phosphate dehydrogenase (GAPDH) were used according to the manufacturer's instructions. Briefly, membranes were incubated with the primary antibody diluted 1:1000 in PBS with 0.5% BSA and 0.1% Tween-20, at 4 °C overnight. After extensive washes, secondary antibodies, goat anti-mouse and goat anti-rabbit HRP-linked, were used at 1:10,000 dilution for 1 h at room temperature. After washing, the specific proteins were detected using an ECL chemiluminescent substrate in a ChemiDoc XRS+ gel imaging system (Biorad). Three independent experiments were performed.

**4.11. In Vivo Pharmacokinetic Analysis.** All animal experiments were conducted in accordance with the institutional guidelines for the care and use of experimental animals of the University of Valladolid (Spain) in accordance with Directive 2010/63/EU (resolution number 2010/2/23).

BALB/c mice aged 14–16 weeks ( $n = 5$  per group) were injected intravenously with 5 mg/Kg fluorescein-labeled ELR nanoparticles. For the time course analysis, 20  $\mu\text{L}$  of blood was collected from the submandibular vein at 1, 2, 3, 4, 5, 6, and 24 h after injection and immediately diluted into 80  $\mu\text{L}$  of heparinized PBS. The blood was centrifuged at  $21100 \times g$  for 10 min at 4 °C, and the supernatant was loaded onto a black clear bottom 96-well plate for fluorescence reading using a SpectraMax M5e microplate reader (Molecular

Devices) with excitation and emission wavelengths of 494 and 518 nm, respectively. Plasma autofluorescence was determined in negative control (non-injected) mice and subtracted to the samples values. Fluorescence intensity values were converted to concentration by extrapolation from a linear standard curve.

To obtain the pharmacokinetic parameters for the compartmental analysis, the data set of each individual mouse was fit to a one-compartment pharmacokinetic model using SAAM II software (University of Washington, USA).

**4.12. *In Vivo* Biodistribution.** BALB/c mice aged 14–16 weeks ( $n = 5$ ) were injected intravenously via the tail vein with 5 mg/Kg of Cy5-labeled nanoparticles. Fluorescence labeling with Cy5 was used for *in vivo* biodistribution assays to get a better resolution with the IVIS imaging system. After 6 h, animals were anaesthetized with isoflurane in oxygen (4% for induction and 1.5% for maintenance) and transferred immediately to the IVIS imaging system with continuous anesthesia during measurement. An untreated mouse was always measured at the same time as a control. Animals were scanned for fluorescence by the IVIS *in vivo* imaging system (Perkin Elmer). Excitation and emission wavelengths used were 650 and 670 nm, respectively. Moreover, the heart, liver, spleen and kidneys were collected and scanned. Fluorescence of the animals was plotted by subtracting background from an untreated mouse.

**4.13. Histopathological Analysis.** The collected liver, spleen, heart, and kidneys from BALB/c mice used for the *in vivo* studies (as described in Section 4.12) were processed with an automatic tissue processor (Leica TP1020) and embedded in paraffin blocks. Tissue sections of 4  $\mu\text{m}$  of each organ were stained with hematoxylin and eosin (H&E) following instructions from the manufacturer. Assessment on key parameters of organ microstructure and physiology (liver: steatosis, lobular inflammation, ballooning, fibrosis, and portal inflammation; spleen: neutrophils, necrosis, and thrombosis; heart: heart myocardial damage; kidneys: glomerular cellularity, tubular vacuolation, interstitial inflammation, interstitial fibrosis, and vessels) were performed at the Royal Free Hospital (London, UK).

**4.14. Statistical Analysis.** Data are reported as mean  $\pm$  SD ( $n = 3$ ). Statistical analysis was performed by variance analysis in combination with a subsequent analysis using the Bonferroni method. A  $p$ -value of less than 0.05 was considered to be statistically significant. \* $p < 0.05$ , \*\* $p < 0.01$ , \*\*\* $p < 0.001$ . Data were handled using the SPSS Statistics software version 20 (IBM).

## ■ ASSOCIATED CONTENT

### Supporting Information

The Supporting Information is available free of charge at <https://pubs.acs.org/doi/10.1021/acsami.1c14592>.

Physicochemical characterization, including HPLC, MALDI-TOF, DSC,  $^1\text{H-NMR}$ , and DLS spectra for all compounds; NP uptake in PDX cells by flow cytometry; optical phase contrast microscopy images for cell morphology studies; pharmacokinetic profiles after systemic administration of nanomaterials in BALB/c mice (PDF)

## ■ AUTHOR INFORMATION

### Corresponding Author

**Pilar Acedo** – Institute for Liver and Digestive Health, Royal Free Hospital Campus, University College London, London NW3 2QG, United Kingdom; [orcid.org/0000-0003-4815-6090](https://orcid.org/0000-0003-4815-6090); Email: [p.nunez@ucl.ac.uk](mailto:p.nunez@ucl.ac.uk)

### Authors

**Juan Gonzalez-Valdivieso** – Smart Biodevices for NanoMed Group, University of Valladolid, Valladolid 47011, Spain; [orcid.org/0000-0001-9007-2312](https://orcid.org/0000-0001-9007-2312)

**Andres Garcia-Sampedro** – Institute for Liver and Digestive Health, Royal Free Hospital Campus, University College

London, London NW3 2QG, United Kingdom; [orcid.org/0000-0002-2286-8623](https://orcid.org/0000-0002-2286-8623)

**Andrew R. Hall** – Institute for Liver and Digestive Health, Royal Free Hospital Campus, University College London, London NW3 2QG, United Kingdom; Sheila Sherlock Liver Centre, Royal Free London NHS Foundation Trust, London NW3 2QG, United Kingdom

**Alessandra Girotti** – BIOFORGE (Group for Advanced Materials and Nanobiotechnology), CIBER-BBN, University of Valladolid, Valladolid 47011, Spain

**Francisco Javier Arias** – Smart Biodevices for NanoMed Group, University of Valladolid, Valladolid 47011, Spain

**Stephen P. Pereira** – Institute for Liver and Digestive Health, Royal Free Hospital Campus, University College London, London NW3 2QG, United Kingdom

Complete contact information is available at:

<https://pubs.acs.org/doi/10.1021/acsami.1c14592>

## Funding

This work was supported by a Pancreatic Cancer UK (PCUK) project grant and funds from the European Social Fund (ESF), the European Regional Development Fund (ERDF), and the MICIUN (grant numbers MAT2016-79435-R, DTS19/00162, and PID2019-106386RB-I00). J.G.V. was supported by the University of Valladolid as well as the Erasmus+ program of the European Union through a travel fellowship for PhD students. S.P.P. was supported by the National Institute for Health Research University College London Hospitals Biomedical Research Centre. P.A. was supported by a Postdoctoral Fellowship from the Ramón Areces Foundation.

## Notes

The authors declare no competing financial interest.

## ■ ACKNOWLEDGMENTS

The authors would like to thank R. Garcia for her technical assistance with polymers bioproduction and R. Alvarez-Delgado for her assistance with animal procedures. The authors would also like to thank Dr. Miguel Fernandez and the animal services at the University of Leon.

## ■ REFERENCES

- (1) Allemani, C.; Matsuda, T.; Di Carlo, V.; Harewood, R.; Matz, M.; Nikšić, M.; Bonaventure, A.; Valkov, M.; Johnson, C. J.; Estève, J.; Ogunbiyi, O. J.; Azevedo, E. S. G.; Chen, W. Q.; Eser, S.; Engholm, G.; Stiller, C. A.; Monnereau, A.; Woods, R. R.; Visser, O.; Lim, G. H.; Aitken, J.; Weir, H. K.; Coleman, M. P. Global Surveillance of Trends in Cancer Survival 2000–14 (Concord-3): Analysis of Individual Records for 37 513 025 Patients Diagnosed with One of 18 Cancers from 322 Population-Based Registries in 71 Countries. *Lancet*. **2018**, *391*, 1023–1075.
- (2) Bray, F.; Ferlay, J.; Soerjomataram, I.; Siegel, R. L.; Torre, L. A.; Jemal, A. Global Cancer Statistics 2018: Globocan Estimates of Incidence and Mortality Worldwide for 36 Cancers in 185 Countries. *CA Cancer J. Clin.* **2018**, *68*, 394–424.
- (3) Kamisawa, T.; Wood, L. D.; Itoi, T.; Takaori, K. Pancreatic Cancer. *Lancet*. **2016**, *388*, 73–85.
- (4) Labib, P. L.; Goodchild, G.; Pereira, S. P. Molecular Pathogenesis of Cholangiocarcinoma. *BMC Cancer*. **2019**, *19*, 185.
- (5) Pereira, S. P.; Oldfield, L.; Ney, A.; Hart, P. A.; Keane, M. G.; Pandol, S. J.; Li, D.; Greenhalf, W.; Jeon, C. Y.; Koay, E. J.; Almaro, C. V.; Halloran, C.; Lennon, A. M.; Costello, E. Early Detection of Pancreatic Cancer. *Lancet Gastroenterol. Hepatol.* **2020**, *5*, 698–710.
- (6) Neoptolemos, J. P.; Kleeff, J.; Michl, P.; Costello, E.; Greenhalf, W.; Palmer, D. H. Therapeutic Developments in Pancreatic Cancer:

Current and Future Perspectives. *Nat. Rev. Gastroenterol. Hepatol.* **2018**, *15*, 333–348.

(7) Strobel, O.; Neoptolemos, J.; Jäger, D.; Büchler, M. W. Optimizing the Outcomes of Pancreatic Cancer Surgery. *Nat. Rev. Clin. Oncol.* **2019**, *16*, 11–26.

(8) Han, W.; Chilkoti, A.; López, G. P. Self-Assembled Hybrid Elastin-Like Polypeptide/Silica Nanoparticles Enable Triggered Drug Release. *Nanoscale* **2017**, *9*, 6178–6186.

(9) Ryu, J. S.; Raucher, D. Elastin-Like Polypeptide for Improved Drug Delivery for Anticancer Therapy: Preclinical Studies and Future Applications. *Expert Opin. Drug Deliv.* **2015**, *12*, 653–667.

(10) MacEwan, S. R.; Chilkoti, A. Applications of Elastin-Like Polypeptides in Drug Delivery. *J. Controlled Release* **2020**, *26*, 314–7146.

(11) Arias, F. J.; Santos, M.; Ibanez-Fonseca, A.; Pina, M. J.; Serrano, S. Elastin-Like Recombinamers as Smart Drug Delivery Systems. *Curr. Drug Targets* **2018**, *19*, 360–379.

(12) Fernandez-Colino, A.; Quinteros, D. A.; Allemandi, D. A.; Girotti, A.; Palma, S. D.; Arias, F. J. Self-Assembling Elastin-Like Hydrogels for Timolol Delivery: Development of an Ophthalmic Formulation against Glaucoma. *Mol. Pharmaceutics* **2017**, *14*, 4498–4508.

(13) Gonzalez-Valdivieso, J.; Borrego, B.; Girotti, A.; Moreno, S.; Brun, A.; Bermejo-Martin, J. F.; Arias, F. J. A DNA Vaccine Delivery Platform Based on Elastin-Like Recombinamer Nanosystems for Rift Valley Fever Virus. *Mol. Pharmaceutics* **2020**, *17*, 1608–1620.

(14) Vallejo, R.; Gonzalez-Valdivieso, J.; Santos, M.; Rodriguez-Rojo, S.; Arias, F. J. Production of Elastin-Like Recombinamer-Based Nanoparticles for Docetaxel Encapsulation and Use as Smart Drug-Delivery Systems Using a Supercritical Anti-Solvent Process. *J. Ind. Eng. Chem.* **2021**, *93*, 361–374.

(15) Spencer, D. S.; Puranik, A. S.; Peppas, N. A. Intelligent Nanoparticles for Advanced Drug Delivery in Cancer Treatment. *Curr. Opin. Chem. Eng.* **2015**, *7*, 84–92.

(16) Gonzalez-Valdivieso, J.; Girotti, A.; Schneider, J.; Arias, F. J. Advanced Nanomedicine and Cancer: Challenges and Opportunities in Clinical Translation. *Int. J. Pharm.* **2021**, *599*, 120438–120446.

(17) Quader, S.; Kataoka, K. Nanomaterial-Enabled Cancer Therapy. *Mol. Ther.* **2017**, *25*, 1501–1513.

(18) Matsumura, Y.; Maeda, H. A New Concept for Macromolecular Therapeutics in Cancer Chemotherapy: Mechanism of Tumoritropic Accumulation of Proteins and the Antitumor Agent Smancs. *Cancer Res.* **1986**, *46*, 6387–6392.

(19) Maeda, H.; Bharate, G. Y.; Daruwalla, J. Polymeric Drugs for Efficient Tumor-Targeted Drug Delivery Based on EPR-Effect. *Eur. J. Pharm. Biopharm.* **2009**, *71*, 409–419.

(20) Byrne, J. D.; Betancourt, T.; Brannon-Peppas, L. Active Targeting Schemes for Nanoparticle Systems in Cancer Therapeutics. *Adv. Drug Delivery Rev.* **2008**, *60*, 1615–1626.

(21) Trabulo, S.; Aires, A.; Aicher, A.; Heeschen, C.; Cortajarena, A. L. Multifunctionalized Iron Oxide Nanoparticles for Selective Targeting of Pancreatic Cancer Cells. *Biochim. Biophys. Acta Gen. Subj.* **2017**, *1861*, 1597–1605.

(22) Luo, J.; Manning, B. D.; Cantley, L. C. Targeting the PI3K-Akt Pathway in Human Cancer: Rationale and Promise. *Cancer Cell* **2003**, *4*, 257–262.

(23) Cantley, L. C. The Phosphoinositide 3-Kinase Pathway. *Science* **2002**, *296*, 1655–1657.

(24) Song, M.; Bode, A. M.; Dong, Z.; Lee, M. H. Akt as a Therapeutic Target for Cancer. *Cancer Res.* **2019**, *79*, 1019–1031.

(25) Massihnia, D.; Avan, A.; Funel, N.; Maftouh, M.; van Krieken, A.; Granchi, C.; Raktoe, R.; Boggi, U.; Aicher, B.; Minutolo, F.; Russo, A.; Leon, L. G.; Peters, G. J.; Giovannetti, E. Phospho-Akt Overexpression Is Prognostic and Can Be Used to Tailor the Synergistic Interaction of Akt Inhibitors with Gemcitabine in Pancreatic Cancer. *J. Hematol. Oncol.* **2017**, *10*, 9.

(26) Bellacosa, A.; Testa, J. R.; Staal, S. P.; Tsichlis, P. N. A Retroviral Oncogene, Akt, Encoding a Serine-Threonine Kinase Containing an Sh2-Like Region. *Science* **1991**, *254*, 274–277.

(27) Hirata, N.; Suizu, F.; Matsuda-Lennikov, M.; Edamura, T.; Bala, J.; Noguchi, M. Inhibition of Akt Kinase Activity Suppresses Entry and Replication of Influenza Virus. *Biochem. Biophys. Res. Commun.* **2014**, *450*, 891–898.

(28) Hiromura, M.; Okada, F.; Obata, T.; Auguin, D.; Shibata, T.; Roumestand, C.; Noguchi, M. Inhibition of Akt Kinase Activity by a Peptide Spanning the Betaa Strand of the Proto-Oncogene Tc1. *J. Biol. Chem.* **2004**, *279*, 53407–53418.

(29) Rubio-Viqueira, B.; Jimeno, A.; Cusatis, G.; Zhang, X.; Iacobuzio-Donahue, C.; Karikari, C.; Shi, C.; Danenberg, K.; Danenberg, P. V.; Kuramochi, H.; Tanaka, K.; Singh, S.; Salimi-Moosavi, H.; Bouraoud, N.; Amador, M. L.; Altiok, S.; Kulesza, P.; Yeo, C.; Messersmith, W.; Eshleman, J.; Hruban, R. H.; Maitra, A.; Hidalgo, M. An In Vivo Platform for Translational Drug Development in Pancreatic Cancer. *Clin. Cancer Res.* **2006**, *12*, 4652–4661.

(30) Rubio-Viqueira, B.; Hidalgo, M. Direct in Vivo Xenograft Tumor Model for Predicting Chemotherapeutic Drug Response in Cancer Patients. *Clin. Pharmacol. Ther.* **2009**, *85*, 217–221.

(31) Hidalgo, M.; Amant, F.; Biankin, A. V.; Budinska, E.; Byrne, A. T.; Caldas, C.; Clarke, R. B.; de Jong, S.; Jonkers, J.; Maelandsmo, G. M.; Roman-Roman, S.; Seoane, J.; Trusoloni, L.; Villanueva, A. Patient-Derived Xenograft Models: An Emerging Platform for Translational Cancer Research. *Cancer Discov.* **2014**, *4*, 998–1013.

(32) Aparicio, S.; Hidalgo, M.; Kung, A. L. Examining the Utility of Patient-Derived Xenograft Mouse Models. *Nat. Rev. Cancer.* **2015**, *15*, 311–316.

(33) Shi, L.; Wang, Y.; Wang, Q.; Jiang, Z.; Ren, L.; Yan, Y.; Liu, Z.; Wan, J.; Huang, L.; Cen, B.; Han, W.; Wang, H. Transforming a Toxic Drug into an Efficacious Nanomedicine Using a Lipoprodrug Strategy for the Treatment of Patient-Derived Melanoma Xenografts. *J. Controlled Release* **2020**, *324*, 289–302.

(34) Huang, L.; Chen, X.; Bian, Q.; Zhang, F.; Wu, H.; Wang, H.; Gao, J. Photosensitizer-Stabilized Self-Assembling Nanoparticles Potentiate Chemo/Photodynamic Efficacy of Patient-Derived Melanoma. *J. Controlled Release* **2020**, *328*, 325–338.

(35) Gonzalez-Valdivieso, J.; Girotti, A.; Munoz, R.; Rodriguez-Cabello, J. C.; Arias, F. J. Self-Assembling Elr-Based Nanoparticles as Smart Drug-Delivery Systems Modulating Cellular Growth Via Akt. *Biomacromolecules* **2019**, *20*, 1996–2007.

(36) Garcia-Arevalo, C.; Bermejo-Martin, J. F.; Rico, L.; Iglesias, V.; Martin, L.; Rodriguez-Cabello, J. C.; Arias, F. J. Immunomodulatory Nanoparticles from Elastin-Like Recombinamers: Single-Molecules for Tuberculosis Vaccine Development. *Mol. Pharmaceutics* **2013**, *10*, 586–597.

(37) Ohmori, N.; Niidome, T.; Wada, A.; Hirayama, T.; Hatakeyama, T.; Aoyagi, H. The Enhancing Effect of Anionic Alpha-Helical Peptide on Cationic Peptide-Mediated Transfection Systems. *Biochem. Biophys. Res. Commun.* **1997**, *235*, 726–729.

(38) Kirana, C.; Shi, H.; Laing, E.; Hood, K.; Miller, R.; Bethwaite, P.; Keating, J.; Jordan, T. W.; Hayes, M.; Stubbs, R. Cathepsin D Expression in Colorectal Cancer: From Proteomic Discovery through Validation Using Western Blotting, Immunohistochemistry, and Tissue Microarrays. *Int. J. Proteomics.* **2012**, *2012*, 245819.

(39) Bure, C.; Maget, R.; Delmas, A. F.; Pichon, C.; Midoux, P. Histidine-Rich Peptide: Evidence for a Single Zinc-Binding Site on H5wyg Peptide That Promotes Membrane Fusion at Neutral Ph. *J. Mass Spectrom.* **2009**, *44*, 81–89.

(40) Li, Y.; Gu, N. Thermodynamics of Charged Nanoparticle Adsorption on Charge-Neutral Membranes: A Simulation Study. *J. Phys. Chem. B.* **2010**, *114*, 2749–2754.

(41) Lin, J.; Zhang, H.; Chen, Z.; Zheng, Y. Penetration of Lipid Membranes by Gold Nanoparticles: Insights into Cellular Uptake, Cytotoxicity, and Their Relationship. *ACS Nano* **2010**, *4*, 5421–5429.

(42) Malam, Y.; Loizidou, M.; Seifalian, A. M. Liposomes and Nanoparticles: Nanosized Vehicles for Drug Delivery in Cancer. *Trends Pharmacol. Sci.* **2009**, *30*, 592–599.

(43) Arvizo, R. R.; Miranda, O. R.; Thompson, M. A.; Pabelick, C. M.; Bhattacharya, R.; Robertson, J. D.; Rotello, V. M.; Prakash, Y. S.;

Mukherjee, P. Effect of Nanoparticle Surface Charge at the Plasma Membrane and Beyond. *Nano Lett.* **2010**, *10*, 2543–2548.

(44) Garcia, P. L.; Miller, A. L.; Yoon, K. J. Patient-Derived Xenograft Models of Pancreatic Cancer: Overview and Comparison with Other Types of Models. *Cancers* **2020**, *12*, 1327.

(45) Hwang, C. I.; Boj, S. F.; Clevers, H.; Tuveson, D. A. Preclinical Models of Pancreatic Ductal Adenocarcinoma. *J. Pathol.* **2016**, *238*, 197–204.

(46) GEPIA. <http://gepia.cancer-pku.cn> (accessed 2021-05-26).

(47) Mantovani, A. Molecular Pathways Linking Inflammation and Cancer. *Curr. Mol. Med.* **2010**, *10*, 369–373.

(48) Huang, Q.; Zhan, L.; Cao, H.; Li, J.; Lyu, Y.; Guo, X.; Zhang, J.; Ji, L.; Ren, T.; An, J.; Liu, B.; Nie, Y.; Xing, J. Increased Mitochondrial Fission Promotes Autophagy and Hepatocellular Carcinoma Cell Survival through the Ros-Modulated Coordinated Regulation of the Nfkb and Tp53 Pathways. *Autophagy* **2016**, *12*, 999–1014.

(49) Savitskaya, M. A.; Onishchenko, G. E. Mechanisms of Apoptosis. *Biochemistry* **2015**, *80*, 1393–1405.

(50) Zhao, H. F.; Wang, J.; Tony To, S. S. The Phosphatidylinositol 3-Kinase/Akt and C-Jun N-Terminal Kinase Signaling in Cancer: Alliance or Contradiction? (Review). *Int. J. Oncol.* **2015**, *47*, 429–436.

(51) Choi, Y.; Ko, Y. S.; Park, J.; Choi, Y.; Kim, Y.; Pyo, J. S.; Jang, B. G.; Hwang, D. H.; Kim, W. H.; Lee, B. L. Her2-Induced Metastasis Is Mediated by Akt/Jnk/Emt Signaling Pathway in Gastric Cancer. *World J. Gastroenterol.* **2016**, *22*, 9141–9153.

(52) Raucher, D.; Massodi, I.; Bidwell, G. L. Thermally Targeted Delivery of Chemotherapeutics and Anti-Cancer Peptides by Elastin-Like Polypeptide. *Expert Opin. Drug Deliv.* **2008**, *5*, 353–369.

(53) MacKay, J. A.; Chen, M.; McDaniel, J. R.; Liu, W.; Simnick, A. J.; Chilkoti, A. Self-Assembling Chimeric Polypeptide-Doxorubicin Conjugate Nanoparticles That Abolish Tumours after a Single Injection. *Nat. Mater.* **2009**, *8*, 993–999.

(54) Lee, C.; Guo, H.; Klinngam, W.; Janga, S. R.; Yarber, F.; Peddi, S.; Edman, M. C.; Tiwari, N.; Liu, S.; Louie, S. G.; Hamm-Alvarez, S. F.; MacKay, J. A. Berunda Polypeptides: Biheaded Rapamycin Carriers for Subcutaneous Treatment of Autoimmune Dry Eye Disease. *Mol. Pharmaceutics* **2019**, *16*, 3024–3039.

(55) Shi, P.; Aluri, S.; Lin, Y. A.; Shah, M.; Edman, M.; Dhandhukia, J.; Cui, H.; MacKay, J. A. Elastin-Based Protein Polymer Nanoparticles Carrying Drug at Both Corona and Core Suppress Tumor Growth in Vivo. *J. Controlled Release* **2013**, *171*, 330–338.

(56) Hu, J.; Wang, G.; Liu, X.; Gao, W. Enhancing Pharmacokinetics, Tumor Accumulation, and Antitumor Efficacy by Elastin-Like Polypeptide Fusion of Interferon Alpha. *Adv. Mater.* **2015**, *27*, 7320–7324.

(57) Bergin, I. L.; Witzmann, F. A. Nanoparticle Toxicity by the Gastrointestinal Route: Evidence and Knowledge Gaps. *Int. J. Biomed. Nanosci. Nanotechnol.* **2013**, *3*, 163.

(58) Walczak, A. P.; Kramer, E.; Hendriksen, P. J.; Helsdingen, R.; van der Zande, M.; Rietjens, I. M.; Bouwmeester, H. In Vitro Gastrointestinal Digestion Increases the Translocation of Polystyrene Nanoparticles in an in Vitro Intestinal Co-Culture Model. *Nanotoxicology* **2015**, *9*, 886–894.

(59) des Rieux, A.; Ragnarsson, E. G.; Gullberg, E.; Preat, V.; Schneider, Y. J.; Artursson, P. Transport of Nanoparticles across an in Vitro Model of the Human Intestinal Follicle Associated Epithelium. *Eur. J. Pharm. Sci.* **2005**, *25*, 455–465.

(60) Crater, J. S.; Carrier, R. L. Barrier Properties of Gastrointestinal Mucus to Nanoparticle Transport. *Macromol. Biosci.* **2010**, *10*, 1473–1483.

(61) Yang, D.; Liu, D.; Qin, M.; Chen, B.; Song, S.; Dai, W.; Zhang, H.; Wang, X.; Wang, Y.; He, B.; Tang, X.; Zhang, Q. Intestinal Mucin Induces More Endocytosis but Less Transcytosis of Nanoparticles across Enterocytes by Triggering Nanoclustering and Strengthening the Retrograde Pathway. *ACS Appl. Mater. Interfaces* **2018**, *10*, 11443–11456.

(62) Shi, J.; Kantoff, P. W.; Wooster, R.; Farokhzad, O. C. Cancer Nanomedicine: Progress, Challenges and Opportunities. *Nat. Rev. Cancer.* **2017**, *17*, 20–37.

(63) Behzadi, S.; Serpooshan, V.; Tao, W.; Hamaly, M. A.; Alkawareek, M. Y.; Dreaden, E. C.; Brown, D.; Alkilany, A. M.; Farokhzad, O. C.; Mahmoudi, M. Cellular Uptake of Nanoparticles: Journey inside the Cell. *Chem. Soc. Rev.* **2017**, *46*, 4218–4244.

(64) Rossi, M. L.; Rehman, A. A.; Gondi, C. S. Therapeutic Options for the Management of Pancreatic Cancer. *World J. Gastroenterol.* **2014**, *20*, 11142–11159.

(65) Kleiner, D. E.; Brunt, E. M.; Van Natta, M.; Behling, C.; Contos, M. J.; Cummings, O. W.; Ferrell, L. D.; Liu, Y. C.; Torbenson, M. S.; Unalp-Arida, A.; Yeh, M.; McCullough, A. J.; Sanyal, A. J. Design and Validation of a Histological Scoring System for Nonalcoholic Fatty Liver Disease. *Hepatology.* **2005**, *41*, 1313–1321.

(66) Gibson-Corley, K. N.; Olivier, A. K.; Meyerholz, D. K. Principles for Valid Histopathologic Scoring in Research. *Vet. Pathol.* **2013**, *50*, 1007–1015.

(67) Sachdeva, J.; Dai, W.; Kloner, R. A. Functional and Histological Assessment of an Experimental Model of Takotsubo's Cardiomyopathy. *J. Am. Heart Assoc.* **2014**, *3*, No. e000921.

(68) Courtois, S.; de Luxan-Delgado, B.; Penin-Peyta, L.; Royo-Garcia, A.; Parejo-Alonso, B.; Jagust, P.; Alcalá, S.; Rubiolo, J. A.; Sanchez, L.; Sainz, B.; Heeschen, C.; Sancho, P. Inhibition of Mitochondrial Dynamics Preferentially Targets Pancreatic Cancer Cells with Enhanced Tumorigenic and Invasive Potential. *Cancers* **2021**, *13*, 698.

(69) Rodriguez-Cabello, J. C.; Girotti, A.; Ribeiro, A.; Arias, F. J. Synthesis of Genetically Engineered Protein Polymers (Recombinamers) as an Example of Advanced Self-Assembled Smart Materials. *Methods Mol. Biol.* **2012**, *811*, 17–38.

(70) Sallach, R. E.; Cui, W.; Balderrama, F.; Martinez, A. W.; Wen, J.; Haller, C. A.; Taylor, J. V.; Wright, E. R.; Long, R. C., Jr.; Chaikof, E. L. Long-Term Biostability of Self-Assembling Protein Polymers in the Absence of Covalent Crosslinking. *Biomaterials* **2010**, *31*, 779–791.

# **Supporting Information**

## **Smart nanoparticles as advanced anti-Akt kinase delivery systems for pancreatic cancer therapy**

Juan Gonzalez-Valdivieso<sup>1</sup>, Andres Garcia-Sampedro<sup>2</sup>, Andrew R. Hall<sup>2,3</sup>, Alessandra Girotti<sup>4</sup>, Francisco Javier Arias<sup>1</sup>, Stephen P. Pereira<sup>2</sup> and Pilar Acedo<sup>2\*</sup>

<sup>1</sup>Smart Biodevices for NanoMed Group, University of Valladolid, Paseo Belén, 47011, Valladolid, Spain

<sup>2</sup>Institute for Liver and Digestive Health, Royal Free Hospital, University College London, Pond Street, NW3 2QG, London, United Kingdom

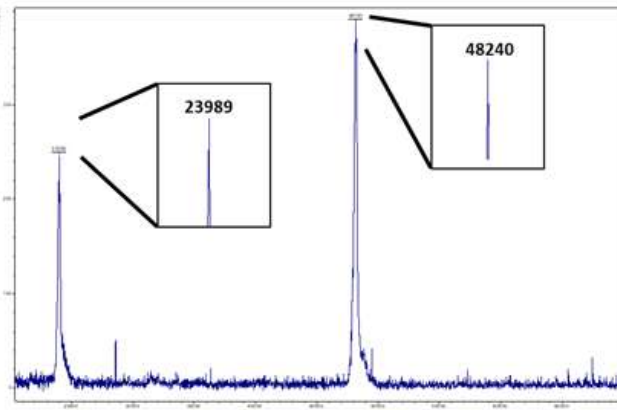
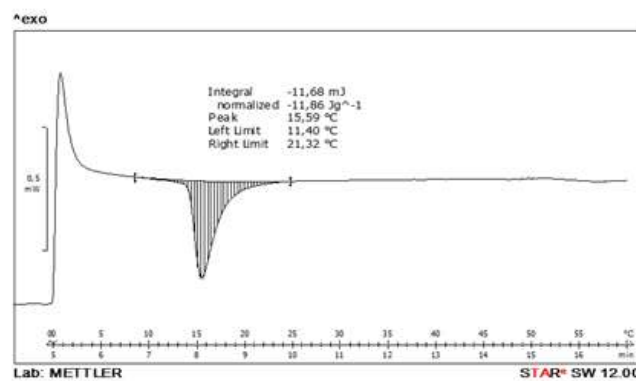
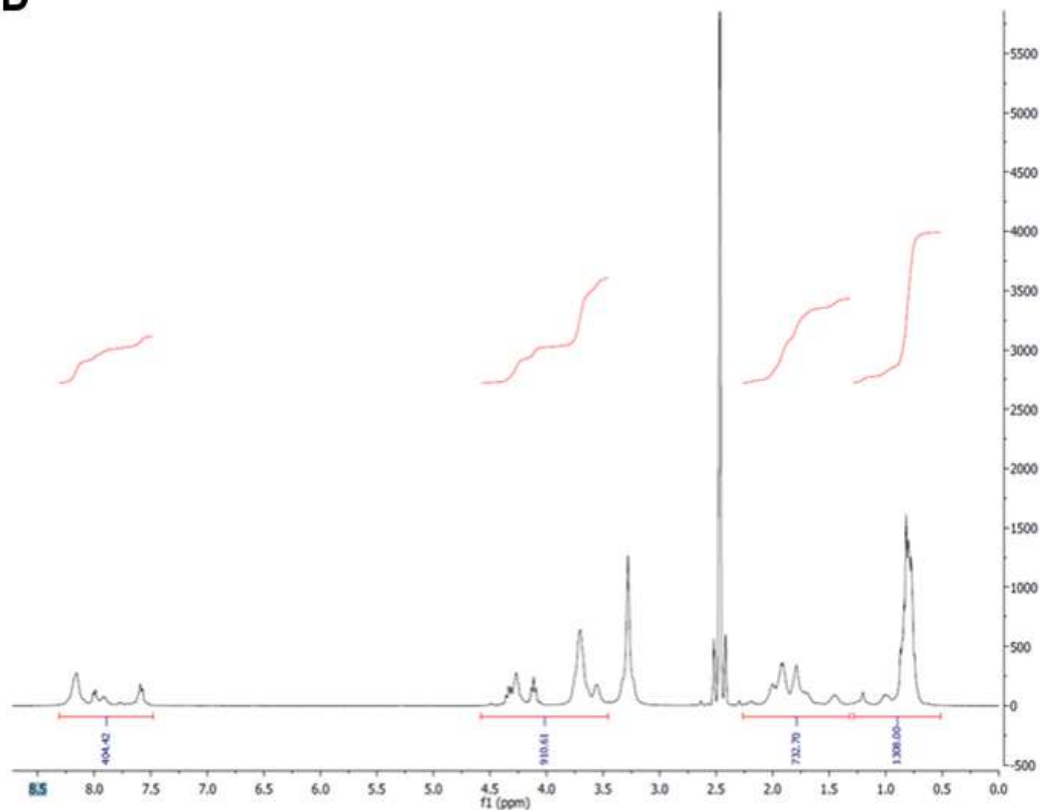
<sup>3</sup>Sheila Sherlock Liver Centre, Royal Free London NHS Foundation Trust, NW3 2QG, London, United Kingdom

<sup>4</sup>BIOFORGE (Group for Advanced Materials and Nanobiotechnology), CIBER-BBN, University of Valladolid, Paseo Belén, 47011, Valladolid, Spain

\*Corresponding author: p.nunez@ucl.ac.uk

**A**

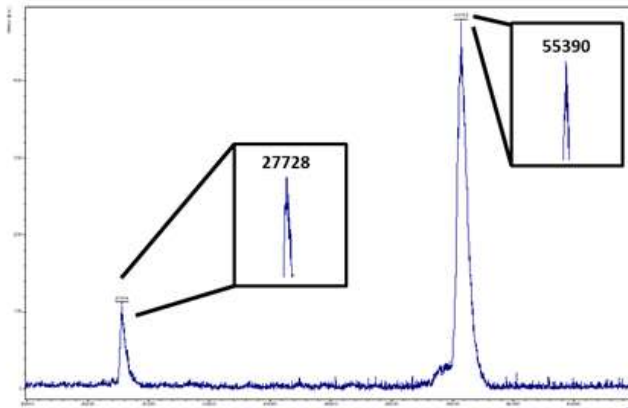
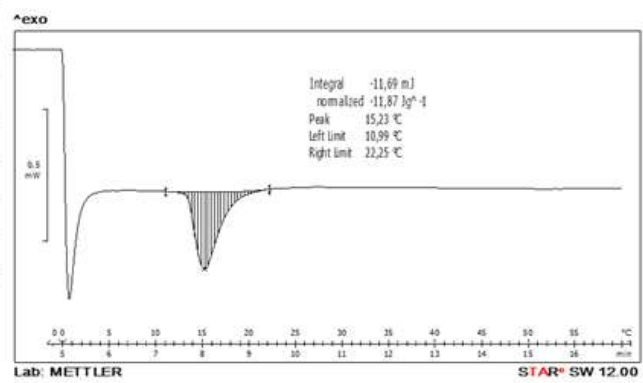
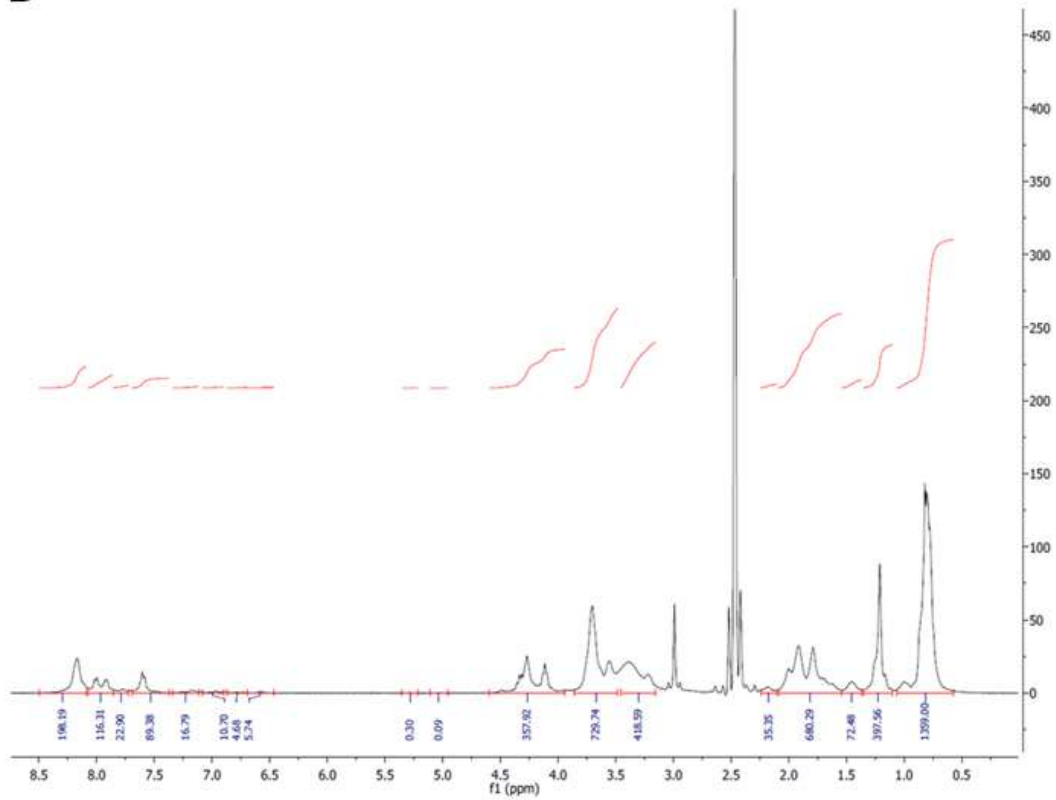
Amino acid	Theoretical	Experimental
Asp+Asn		
Glu+Gln	13	12.73
Ser		
His		
Gly	220	218.91
Thr		
Arg		
Ala	3	4.23
Tyr		
Cys		
Val	150	149.53
Met		
Trp		
Phe		
Ile	60	61.15
Leu	6	6.20
Lys	3	2.90
Pro	110	109.41

**B****C****D**

**Figure S1.** Physicochemical characterisation of control ELR. A: The amino acid composition was verified by high performance liquid chromatography (HPLC). B: The molecular weight of the recombinamer was determined by mass spectrometry (MALDI-TOF/MS). MALDI-TOF spectrum represents non-quantitative intensity (a.u.) against  $m/z$  (mass divided by net charge of the molecule) of the ELR. Both the mono charged (48163) and the doubly charged (23989) ELRs were detected. The theoretical molecular weight was 48250 Da. All experimental values were in accordance with the theoretical ones, being the differences within the instrumental error of the techniques. C: Determination of transition temperature ( $T_t$ ) by differential scanning calorimetry (DSC) in PBS (pH 7.4). The  $T_t$  was 15.59°C. D: The purity of control polymer was corroborated by  $^1\text{H-NMR}$  spectrum. Experimental values were found by taking  $-\text{CH}_3$  as reference.

**A**

Amino acid	Theoretical	Experimental
Asp+Asn	3	3.14
Glu+Gln	16	15.14
Ser		
His	6	5.31
Gly	252	252.78
Thr	1	1.25
Arg	2	2.01
Ala	7	6.71
Tyr	3	3.32
Cys		
Val	157	154.72
Met		
Trp	4	3.83
Phe	3	3.04
Ile	63	64.35
Leu	9	9.83
Lys	3	2.89
Pro	111	109.77

**B****C****D**

**Figure S2.** Physicochemical characterisation of Akt-in ELR. A: The amino acid composition was verified by high performance liquid chromatography (HPLC). B: The molecular weight of the recombinamer was determined by mass spectrometry (MALDI-TOF/MS). MALDI-TOF spectrum represents non-quantitative intensity (a.u.) against  $m/z$  (mass divided by net charge of the molecule) of the ELR. Both the mono charged (55390) and the doubly charged (27728) ELRs were detected. The theoretical molecular weight was 55330 Da. All experimental values were in accordance with the theoretical ones, being the differences within the instrumental error of the techniques C: Determination of transition temperature ( $T_t$ ) by differential scanning calorimetry (DSC) in PBS (pH 7.4). The  $T_t$  was 15.23°C. D: The purity of control polymer was corroborated by  $^1\text{H-NMR}$  spectrum. Experimental values were found by taking  $-\text{CH}_3$  as reference.

**Table S1.** Comparison between the predicted value of each type of hydrogen in the ELRs used in this study and the experimental values found by integration of each peak in the corresponding  $^1\text{H-NMR}$  spectrum (Fig. S2D and S3D). The purity of control polymer was corroborated by  $^1\text{H-NMR}$  spectrum. Experimental values were found by taking  $-\text{CH}_3$  as reference, whereas the others experimental proton integrals were compared to theoretical values. Concordance of theoretical and experimental values confirms the correctness of ELRs composition, as well as their purity.

Type of hydrogen	ppm range	Theoretical value		Experimental value	
		Control	Akt-in	Control	Akt-in
$\text{CH}_3$	1	1308	1359	Reference	
$\text{CH}_2$ and CH	1.5	61	61	40.30	72.48
	1.7-2.3	717	717	692.40	715.64
	3.5-4.5	1011	1057	910.61	1087.66
Aromatic CH	7.5	-	66	-	89.38
NH	8	457	502	404.42	514.17

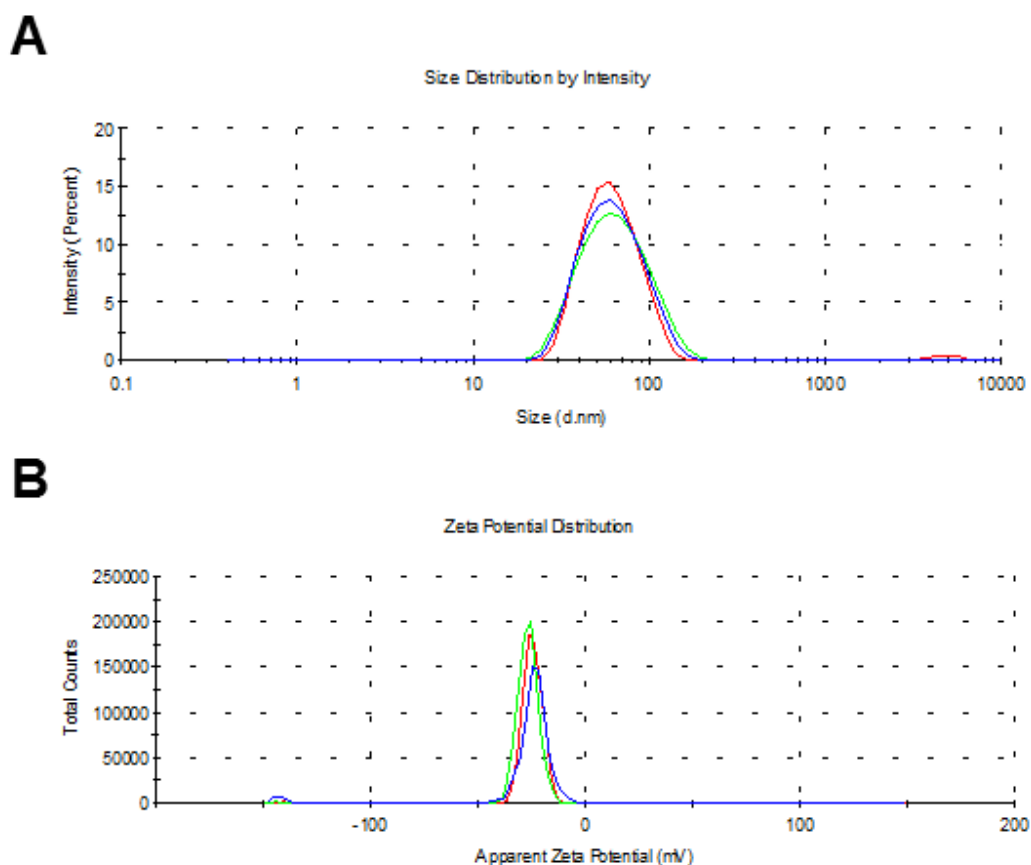


**Figure S3.** Characterisation of 0.5 mg/mL ELR control nanoparticles. **A:** Determination of size by dynamic light scattering (DLS) in PBS buffer (pH 7.4) at 37°C. **B:** Determination of z-potential measured by DLS in ultrapure water type I at 37°C. Control polymer self-assembled into highly monodisperse nanoparticles of  $67.1 \pm 2.5$  nm size, 0.093 polydispersity index and surface charge of -27.6 mV. n=3 independent experiments, mean  $\pm$  SD.

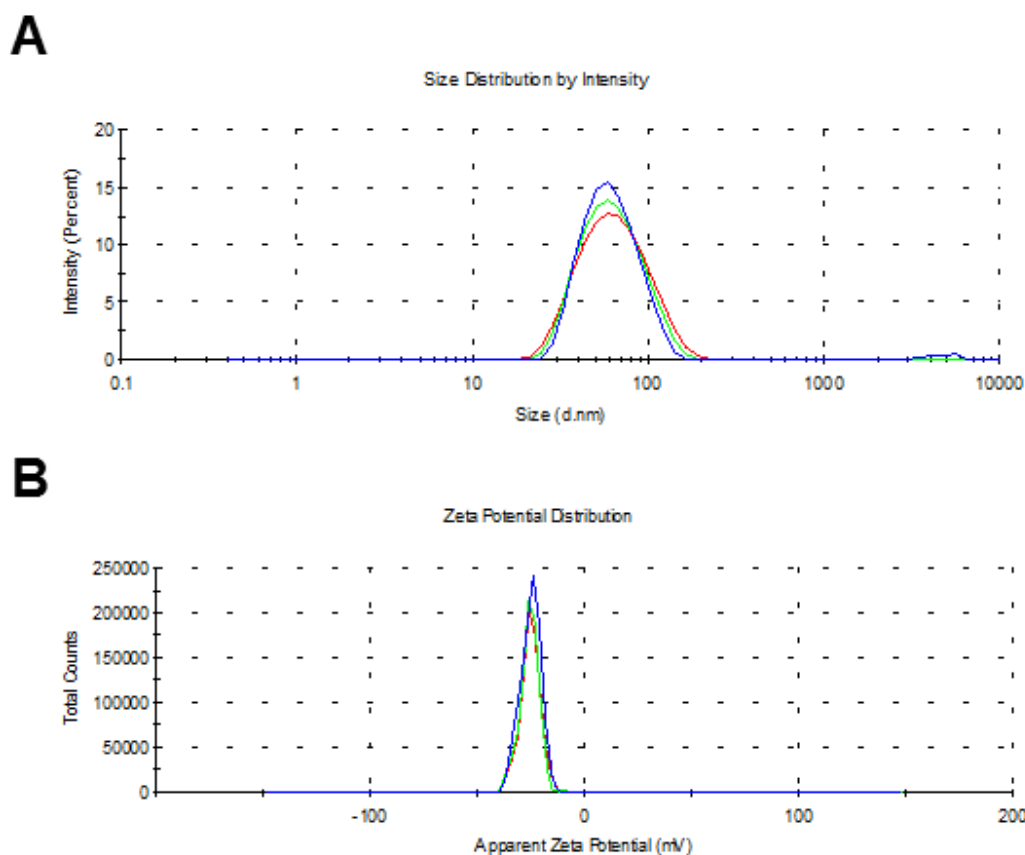


**Figure S4.** Characterisation of 0.5 mg/mL ELR Akt-in nanoparticles. **A:** Determination of size by dynamic light scattering (DLS) in PBS buffer (pH 7.4) at 37°C. **B:** Determination of z-potential measured by DLS in ultrapure water type I at 37°C. Akt-in polymer self-assembled into highly monodisperse nanoparticles of  $73.1 \pm 3.2$  nm size, 0.083 polydispersity index and surface charge of -26.7 mV. n=3 independent experiments, mean  $\pm$  SD.

**Table S2.** Physicochemical characterisation of fluorescently-labelled ELR polymers. Size (diameter) and polydispersity index (PDI) of self-assembled polymers dissolved in PBS and measured at 37°C by dynamic light scattering (DLS). Surface charge of self-assembled polymers dissolved in ultrapure water type I measured by DLS. n=3 independent experiments, mean  $\pm$  SD.

	<b>D<sub>h</sub> (nm)</b>	<b>PdI</b>	<b>ζ-potential (mV)</b>
Fluorescein-control	67.5 $\pm$ 1.9	0.120	-27.8 $\pm$ 1.0
Fluorescein-Akt-in	73.3 $\pm$ 3.0	0.104	-27.2 $\pm$ 0.8
Cy7-control	67.4 $\pm$ 2.6	0.102	-27.9 $\pm$ 1.2
Cy7-Akt-in	72.8 $\pm$ 2.7	0.108	-26.9 $\pm$ 1.3

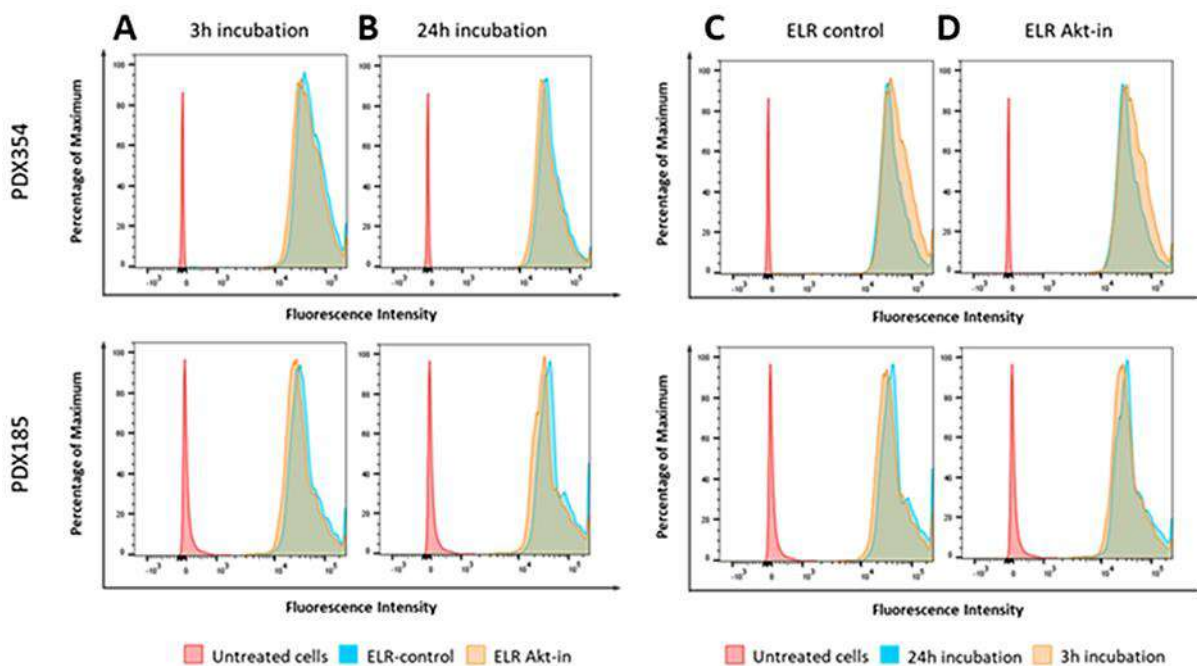


**Figure S5.** Cellular uptake of ELR-based nanoparticles in patient-derived PDX354 and PDX185 cells. A-B: Flow cytometry analysis of cells incubated with 0.5 mg/mL Cy5-labelled control and Akt-in NPs (blue and orange histograms, respectively) for 3 hours (A) or 24 hours (B). n=3 independent experiments. C-D: Flow cytometry time-course analysis of cells incubated with 0.5 mg/mL control (C) or Akt-in (D) Cy5-labelled NPs

for 3 hours (orange histogram) or 24 hours (blue histogram). n=3 independent experiments. Untreated cells are plotted as red histograms.

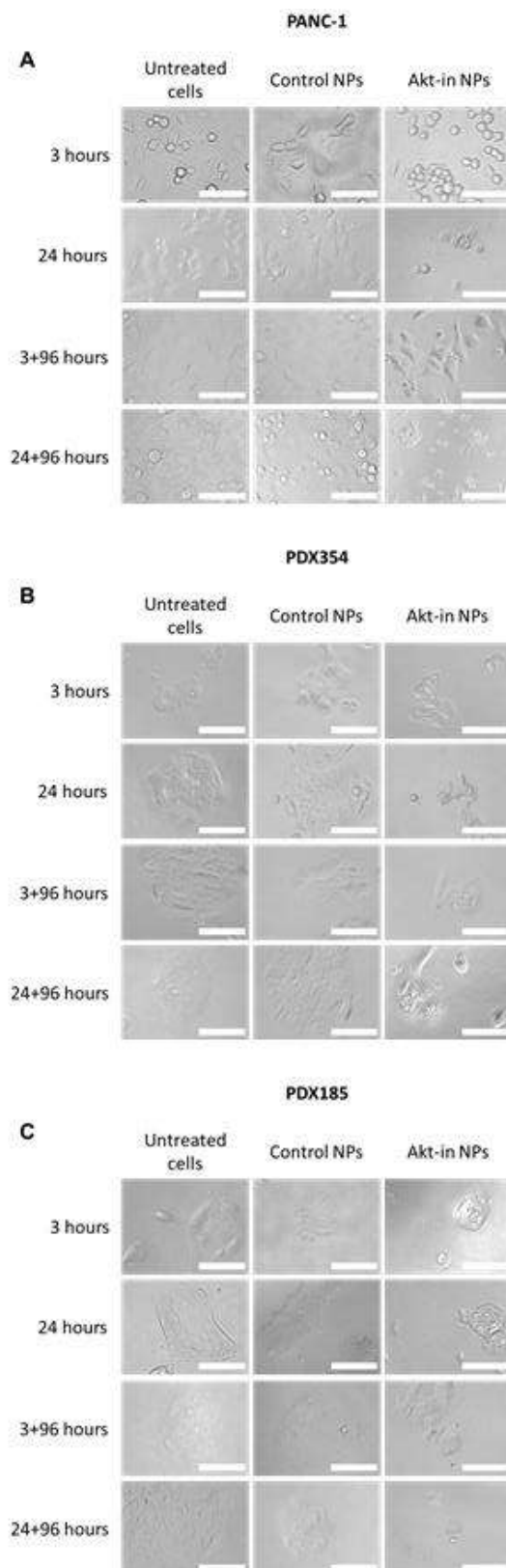


**Figure S6.** Cell morphology of PANC-1 (A), PDX354 (B) and PDX185 (C) cells treated with ELR-based nanoparticles. Cells were incubated with 0.5 mg/mL control and Akt-in nanoparticles for indicated times. From top to bottom: 3 and 24 hours incubation with nanoparticles, 3 and 24 hours incubation with nanoparticles + 96 hours recovery in culture medium without nanoparticles. Pictures were taken by optical phase contrast microscopy. Representative images. Scale bars: 100  $\mu\text{m}$ . n=3 independent experiments.

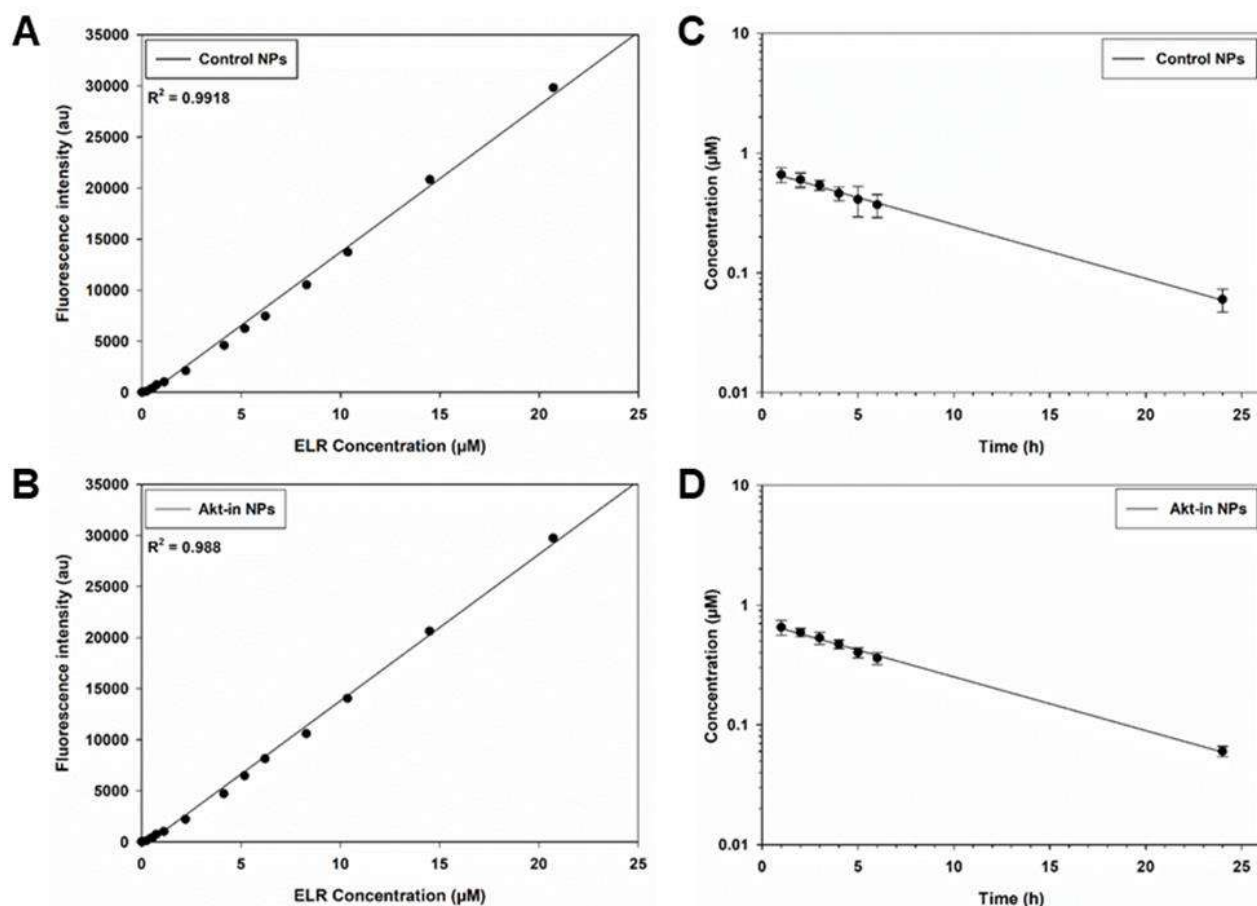


**Figure S7.** Control and Akt-in nanoparticles pharmacokinetic profiles after systemic administration in BALB/c mice. A linear standard curve was achieved by depicting the background-subtracted fluorescence versus the control (A) and Akt-in (B) ELR concentration. Briefly, increasing concentrations of fluorescently-labelled ELR nanoparticles were added to mice plasma and fluorescence intensity was determined. Plasma concentration versus time curve of control (C) and Akt-in (D) nanoparticles after systemic administration to 14-16 week old BALB/c mice (n=5 mice per treatment). Mean  $\pm$  SD.